8-2022

High-Isolation Antenna Technique for CubeSat-Borne, Continuous-Waveform Radar

Logan E. Voigt
Utah State University

Utah State University
MERRILL-CAZIER LIBRARY

HIGH-ISOLATION ANTENNA TECHNIQUE FOR CUBESAT-BORNE,

CONTINUOUS-WAVEFORM RADAR

by

Logan E. Voigt

A thesis submitted in partial fulfillment
of the requirements for the degree

of

MASTER OF SCIENCE

in

Electrical Engineering

Approved:

_____   _____
Reyhan Baktur, Ph.D.   Charles Swenson, Ph.D.
Major Professor   Committee Member

_____   _____
Bryan Willis, Ph.D.   D. Richard Cutler, Ph.D.
Committee Member   Interim Vice Provost of Graduate Studies

UTAH STATE UNIVERSITY
Logan, Utah

2022

ABSTRACT

High-Isolation Antenna Technique for CubeSat-Borne, Continuous-Waveform Radar

by

Logan E. Voigt, Master of Science

Utah State University, 2022

Major Professor: Reyhan Baktur, Ph.D.
Department: Electrical and Computer Engineering

Radar is important in tracking, imaging, and weather prediction applications. As technology is increasingly miniaturized, there is a push for smaller radar. Research and exploration in outer space also benefit from small, low-power technologies. The NASA Jet Propulsion Laboratory's RainCube was the first successful CubeSat-borne radar. CubeSats will benefit from additional research on how to further miniaturize radar payloads.

This thesis demonstrates that implementing a continuous-waveform radar on a CubeSat improves the sensitivity, size, weight, and power consumption of the radar. Integrating the transmit and receive antennas on the solar panels removes the need for antenna-deployment mechanisms and preserves space in a CubeSat. The physical separation between the antennas helps to provide the isolation required for continuous-waveform radar. Designing the antennas with opposite circular polarizations further increases the antenna isolation without weakening the radar return with polarization mismatch. Combining physical-separation and polarization-diversity isolation enables a novel solution to implement a continuous-waveform radar on a small platform, like a CubeSat.

(103 pages)

PUBLIC ABSTRACT

High-Isolation Antenna Technique for CubeSat-Borne, Continuous-Waveform Radar

Logan E. Voigt

Radar is important in target tracking, imaging, and weather prediction applications. As technology is increasingly miniaturized, there is a push for smaller radar. Research and exploration in outer space also benefit from small, low-power technologies. The NASA Jet Propulsion Laboratory's RainCube was the first successful CubeSat-borne radar. A CubeSat is a type of small satellite that conforms to specific size and weight standards. Radar technology benefits from additional research on how to further miniaturize radar payloads.

Integrating the transmit and receive antennas on the solar panels removes the need for antenna-deployment mechanisms, preserving space on the CubeSat. This thesis also demonstrates that implementing a radar that transmits and receives continuously and simultaneously (continuous-waveform) on the CubeSat improves the sensitivity, size, weight, and power consumption of the radar. Continuous-waveform radar suffers from self-interference because the transmitter and receiver are on at the same time.

To overcome the self-interference, the transmitter and receiver must be isolated. Physically separating the antennas helps provide the isolation required for continuous-waveform radar, but is limited by the small size of the CubeSat. Isolation can be further increased by designing the antennas with opposite circular polarizations. The interfering signal traveling directly between the antennas has a different polarization than the receive antenna is designed for, so the interference is suppressed. The signal that hits a target reflects with the opposite circular polarization, so when it arrives at the receiver it has the proper polarization, so it is not suppressed. Combining physical-separation and different-polarization

isolation enables a novel solution to implement a continuous-waveform radar on a small platform like a CubeSat.

Dedicated to my wife, Bryn. Я тебя люблю.

ACKNOWLEDGMENTS

CONTENTS

LIST OF TABLES

LIST OF FIGURES

ACRONYMS

ADC	Analog-to-Digital-Converter
ANT	Antenna
Az	Azimuth
BPF	Band-Pass Filter
CoPol	Co-Polarization
CW	Continuous-Waveform
DAC	Digital-to-Analog-Converter
EM	Electromagnetic
EW	Electronic Warfare
FD	Full-Duplex
FMCW	Frequency-Modulated Continuous-Waveform
GMTI	Ground Moving Target Indication
HPA	High-Power Amplifier
IBFD	In-Band Full-Duplex
JPL	Jet Propulsion Laboratory
LNA	Low-Noise Amplifier
LHCP	Left-Hand Circularly Polarized
LO	Local Oscillator
MIX	Mixer
PDW	Pulse-Doppler Waveform
PRF	Pulse Repetition Frequency
RCS	Radar Cross-Section
RHCP	Right-Hand Circularly Polarized
RF	Radio-Frequency (20 kHz to 300 GHz)
RX	Receiver
SIS	Self-Interference Suppression

SNR	Signal-to-Noise-Ratio
TSI	Time-Separation Isolation
TX	Transmitter
UWB	Ultra-Wideband
VCO	Voltage-Controlled Oscillator
XPol	Cross-Polarization

CHAPTER 1

INTRODUCTION

Radar plays an important role in tracking, imaging, and weather prediction. Since the first satellite-borne radar in 1965 [1], engineers and scientists have worked to improve and miniaturize radar systems to better suit the strict requirements of space. A CubeSat-borne radar provides low-cost capability for monitoring existing space vehicles and debris, tracking objects such as asteroids, remote sensing, and studying space weather.

The first, and currently only, CubeSat-borne radar is the RainCube demonstrated by the NASA Jet Propulsion Laboratory (JPL) in 2018 [2–4]. The RainCube's radar implements a pulse-Doppler waveform (PDW), which has numerous advantages but also suffers from low sensitivity, since pulses reduce the average output power (see Section 2.2.1). To make up for the loss of power from pulsing, PDW radar is designed with high peak output power or high gain antennas. In either case, pulsing draws maximum power while transmitting and much less while receiving. This cyclical change in power usage is an inefficient use of the batteries and decreases their lifespan [5–9].

The limitations of PDW-based radar stem from the requirement that the transmitter (TX) and receiver (RX) be active at different times; otherwise, the TX signal overwhelms the nearby RX, preventing accurate measurements. Alternatively, continuous-waveform (CW) radar transmits and receives continuously and simultaneously. It does not have a duty cycle, which solves the limitation on the output power. It also has less variation in power consumption, which improves battery life. This lifts the requirements for power-hungry and bulky components, promising miniaturization and longer battery life.

A highly accurate CW radar can be realistically designed with two antennas (TX and RX antennas) that are integrated on the solar panels of a CubeSat [10]. A major challenge for CW radar is the required high self-interference suppression (SIS) between the TX and RX.

This research contains three objectives. First, investigate the SIS of opposite circularly polarized antennas integrated on solar panels of a CubeSat. Second, study the design trade-offs to implement an antenna array. Third, build a radar front-end for the high-suppression antennas. These objectives are respectively labeled Objectives 1, 2, and 3.

The novelty of this work is the combination of physical-separation and polarization-diversity suppression techniques to realize CW radar on small platforms. While the CubeSat platform is the focus of this thesis, the design techniques can be applied to other small platforms, such as small aircraft, drones, and portable radar. The following chapters explain why CW radar is the method of choice in this research and how the objectives will be accomplished.

CHAPTER 2

LITERARY REVIEW

Antenna isolation is not a new concept. There have been many studies done to increase isolation between antennas in a variety of ways. This chapter covers radar fundamentals and different types of radar to set the foundation for why CW radar is the radar method of focus in this work. This chapter also explains the extent of the isolation problem and explores common solutions that led to the combination of physical-separation and polarization-diversity isolation.

2.1 Radar Equation

The radar equation [11–13]. describes the received power of a radar signal. The radar equation has different forms depending on which losses are taken into account, which parameters are given, and even the application of the radar [14]. One form is the relationship between the signal-to-noise-ratio (SNR) at the RX to the transmitted power

$$SNR = \frac{P_r}{N} = \frac{P_{\text{avg}} G_t G_r \lambda^2 \sigma}{(4\pi)^3 R_t^2 R_r^2 k_B T_s B_n}, \tag{2.1}$$

where:

$$P_r = \text{received power [W]}$$

$$N = \text{available noise power [W]}$$

$$P_{\text{avg}} = \text{average power transmitted [W]}$$

$$G_t, G_r = \text{gains of the TX and RX antennas}$$

$$\lambda = \text{free-space wavelength [m]}$$

$$\sigma = \text{radar cross-section (RCS) [m}^2\text{]}$$

$$R_t, R_r = \text{ranges from the target to the TX and RX antennas respectively [m]}$$

k_B = Boltzmann constant [Joules/K]

T_s = system noise temperature [K]

B_n = effective bandwidth [Hz].

(2.1) is a general form and takes into account bi-static radar (the TX and RX are separated and use different antennas). If the radar is mono-static (the TX and RX are collocated and share an antenna) then $G_t = G_r$ and $R_t = R_r$.

A larger SNR corresponds to a more sensitive and capable radar. (2.1) shows that the SNR is directly proportional to the average transmitted power. It is then of interest to know how to increase P_{avg}, which is calculated as [11]

$$P_{\text{avg}} = P_t \frac{t_p}{T_r} \tag{2.2}$$

$$= P_t t_p f_r, \tag{2.3}$$

where:

P_t = peak transmit power [W]

t_p = pulse duration [s]

T_r = pulse repetition interval [s]

f_r = pulse repetition frequency (PRF) [Hz].

Thus, increasing peak transmit power, pulse duration, or PRF will increase the average power transmitted.

2.2   Types of Radar

(2.3) applies to any type of radar. Radars can use a variety of signals. The engineer decides what type of signal meets the system requirements. Some common radar signals include pulses, PDW, ultra-wideband (UWB), CW, and frequency-modulated CW (FMCW).

This section briefly introduces these radar waveforms but does not go into detail on the equations and applications for each system. The focus is to compare each system's ability to increase P_{avg}.

2.2.1   Pulse Radar

Pulse radar is the most basic radar. As diagrammed in Figure 2.1, the TX sends a pulse of peak amplitude P_t for t_p seconds. After which time, the TX turns off and the RX turns on and detects the reflected pulse, which has a delay τ. At time T_r the RX turns off and the TX sends out another pulse. The time delay τ from the start of the transmitted pulse to when the RX receives the return signal is used to calculate the target range. Pulse radar is limited to range calculations; it can not determine velocities of targets.
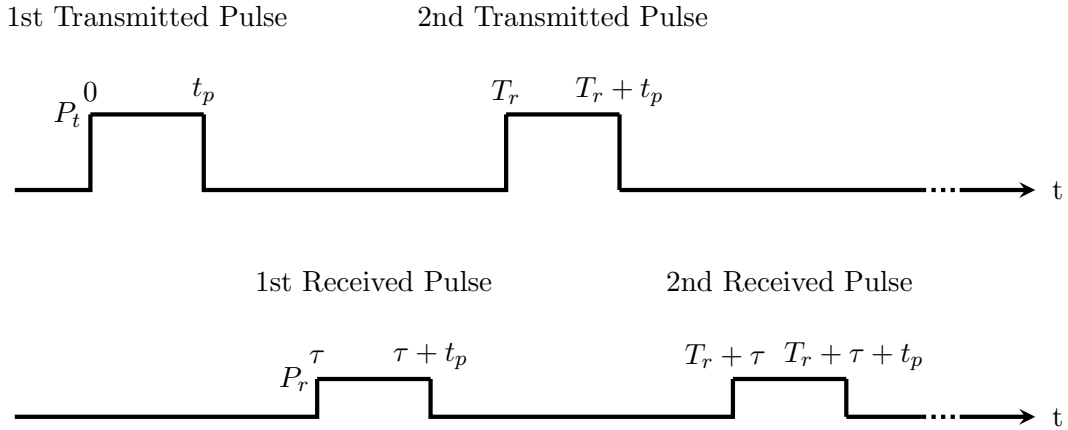
Fig. 2.1: Typical pulse radar.

Pulse radar "listens" for the return only while the TX is off. Increasing t_p or decreasing T_r reduces the time the RX is on. The ratio $\frac{t_p}{T_r}$ is commonly referred to as the duty cycle,

d_t. A smaller d_t corresponds to less transmitted average power.

The PRF sets the processing capabilities of the radar. Low PRF is used for processes that depend on ranging, such as target detection and synthetic aperture radar (SAR) imaging. High PRF is better used for applications that measure target velocity like ground moving target indication (GMTI) [15]. This distinction is the result of ambiguities introduced by the PRF. The lower the PRF the more doppler ambiguities. The higher the PRF the more range ambiguities. If the pulses are sent out too rapidly, when a return pulse is received, it is difficult to determine which of the previous pulses caused this return, and consequently the value of τ and the resulting range calculation are ambiguous [12]. To avoid range ambiguity, designers instead increase P_t to get more average power output.

Hardware puts physical limitations on P_t. Too much power for too long can damage radio-frequency (RF) components in the radar front-end. Hardware that can handle high power is typically heavier, larger, and less efficient. The radar's power supply also suffers from pulsing. Switching back and forth between drawing high current during transmission and low current when receiving decreases the life span of power supplies [5–9]. It is up to the engineer to determine the trade-off between d_t, PRF, and P_t.

In a pulsing scheme, isolation between TX and RX is important. The isolation is different depending on the mode of the radar. While in receiving mode, the RX is highly isolated from the TX because the TX is off. This time separation isolation (TSI) allows the RX to detect weak returns without being overwhelmed by the TX power. Due to TSI, the radar does not require much additional isolation between RX and TX while receiving.

While in transmitting mode, the RX is off, so the TX signal will not interfere with a return signal. However, the front-end components of a radar are designed to receive signals much weaker than the transmit power. If the RX and TX channels are not sufficiently isolated, during transmission the high TX power could overdrive and damage the front-end components [16,17]. Once damaged, these components would not behave as expected in the receiving mode. Thus, even for pulsing radar, isolation between TX and RX is important.

In a bi-static radar, the isolation is achieved by the physical separation between the

TX and RX antennas. For mono-static radar, a circulator provides the isolation (see Section 2.3.3).

2.2.2 Pulse-Doppler Waveform Radar

PDW radar follows the same fundamentals as the pulse radar with the additional capability of measuring target velocities. A PDW radar considers both the delay and frequency of the return pulse. Range is calculated from the delay. Velocity is calculated from the difference between the transmit and receive frequencies (Doppler shift) [11,18].

The same trade-offs between P_t and d_t exists for PDW as for pulse radar. PDW also requires enough isolation during transmission to protect RX front-end components.

2.2.3 Ultra-Wideband Radar

UWB radar uses the scaling relationship between time and bandwidth [14]. A pulse that has a short duration (narrow in time) has a large bandwidth (wide in frequency) and vice versa. Thus, an ultra-wide frequency band corresponds to a very short pulse (shorter than 1 ns) [19]. The power of the UWB signal is spread out over the wide bandwidth, resulting in a very weak return signal. The UWB return signal is integrated at the RX to recover the return.

UWB radar uniquely incorporates low P_t and small d_t. In situations where a radar system needs to be undetectable to other systems, such as electronic warfare (EW) [20–23] or when taking measurements of sensitive biological materials [24,25], UWB radar is advantageous.

2.2.4 Continuous-Waveform

CW radar does not use pulses. The TX and RX operate continuously and simultaneously. The transmitted signal is sinusoidal with one frequency. Since the TX is never off, there is no duty cycle to limit the average power. This results in $P_{\mathrm{avg}} = P_t$, which allows CW radar to transmit a signal with lower peak power and achieve the same or better SNR

than a pulse radar with higher transmit power [11]. This also means that lighter, smaller, and more efficient hardware components can be implemented.

By not having a PRF, CW radar can implement multiple processing schemes simultaneously. Data collected from a CW radar can be separately processed for target detection, image formation, or GMTI by interpreting the data with the necessary PRF. An additional benefit to not having a PRF is the decreased ability that enemy receivers have to detect the radar transmission. This makes CW radar more difficult to jam in EW.

CW radar also has advantages in multi-static configurations. In multi-statics, each radar acts as a transmit or receive node. These nodes add "phase centers" or perspectives to the received data making possible more processing modes like interferometric SAR imaging [26,27]. Multiple TXs and RXs improve sensitivity, target classifications, and EW resistance [28]. A constellation of platforms implementing CW radar could each provide a transmit node, receive node, or both to the multi-static constellation allowing for a large variety of different node configurations.

The consequence of CW radar is that there is no TSI; this puts a stricter requirement on the isolation needed between the TX and RX. There needs to be enough isolation that the RX front-end components are protected. Additionally, there must be enough isolation so that the RX is not saturated by the strong transmitted signal and rendered unable to detect the much weaker radar return. "Self-interference" refers to the condition when the RX is overwhelmed by the TX [29]. In other words, the isolation between TX and RX needs to be high enough to prevent self-interference. In practice CW requires two antennas because transmitting and receiving simultaneously required more dynamic range than can be provided with only one antenna [30].

Additionally, because the transmitted CW signal does not turn on and off, there are no timing cues in the received signal. This makes it impossible to determine the range of a target, yet the Doppler shift can still be determined. For this reason, CW can only measure velocity and not range [11, 31].

2.2.5   Frequency-Modulated Continuous-Waveform

FMCW radar follows the same principles as CW with the additional capability of measuring range. The sinusoidal frequency of the FMCW transmitted signal varies over time. A common form of modulation is linear frequency modulation [1, 32]. This variation of frequency over time allows a delay τ to be measured and utilized to calculate the range [11, 33].

2.3   In-Band Full-Duplex Self-Interference Suppression

In communication systems, the terms full-duplex (FD) and simultaneous-transmit-and-receive refer to a system that can transmit and receive signals at the same time [29, 34–42]. A communications system can be FD by transmitting and receiving at different frequencies. A radar system cannot. The received signal is a reflection of the transmitted signal; hence, the frequency of the RX is dependent on the frequency of the TX.

Communications or radar systems that transmit and receive simultaneously at the same frequency are in-band full-duplex (IBFD) [20, 29, 35–37]. These systems require high SIS. There are two types of SIS: passive isolation between the TX and RX and active cancellation to remove the TX signal from the RX signal. CW radar qualifies as an IBFD system and likewise needs high SIS (see Section 2.2.4).

Sabharwal, et al. [29] identifies three domains in which SIS can occur: Digital domain, Analog-circuit domain, and Propagation domain. These domains are visualized in Figure 2.2
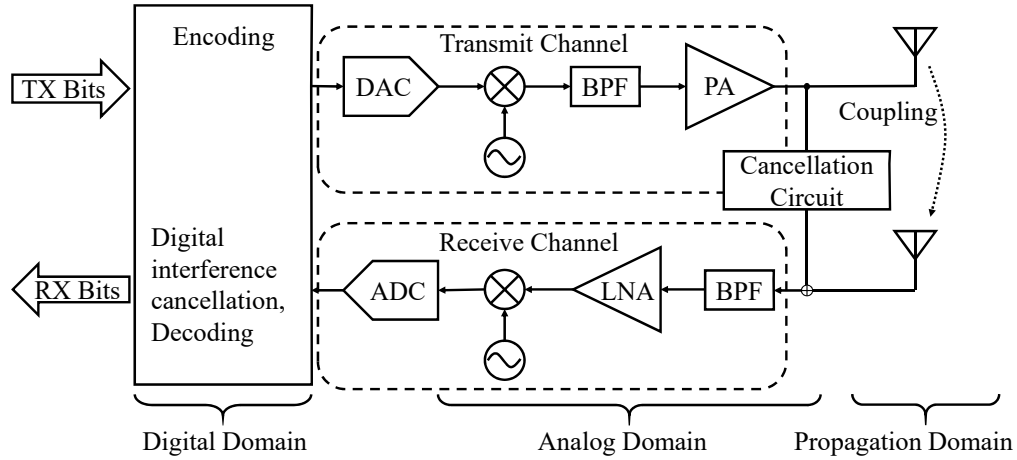
Fig. 2.2: Three domains of SIS.

Sections 2.3.1–2.3.3 define the region each domain includes and presents the amount of SIS typically achievable in each domain.

2.3.1 Digital-Domain SIS

The digital domain is in the RX chain following the analog-to-digital-converter (ADC). In the digital domain, SIS from isolation is impossible because the TX signal interferes with the RX signal in physical space. At the time of digitization, all self-interference has already occurred.

The cancellation possible in the digital domain is limited by the dynamic range of the ADC. The maximum cancellation is equivalent to the dynamic range [29]. If the ADC saturates, cancellation is not possible. Cancellation in the other domains can prevent saturation. It is therefore important to achieve as much cancellation as possible in the analog-circuit and propagation domains.

2.3.2 Analog-Circuit-Domain SIS

The Analog-circuit domain is comprised of the circuitry between the antenna and the ADC. Isolation techniques apply to the analog-circuit domain. Self-interference can be caused by power leakage from the TX channel to the RX channel due to hardware imperfections. Components that are poorly shielded or too close to each other, such as exposed components on a printed circuit board, can radiate energy away from the intended path and be sensed by other components. Additionally, channels that share components (i.e. a circulator; see Section 2.3.3) will have leakage between channels. Analog-circuit-domain isolation decreases these types of leakage.

Cancellation in the analog-circuit domain is accomplished by intentionally tapping energy from the TX channel, feeding it into a cancellation circuit, and combining it with the RX channel [29, 36]. The cancellation circuit adjusts the tapped TX signal to have the same magnitude and opposite phase as the self-interference. Since the magnitude and phase of the interfering signal are unknown, this cancellation is done in a control loop to maximize the cancellation, achieving 15-30 dB of SIS. [29, 34, 43–46]. Sabharwal et al. [29] and Choi et al. [34] demonstrate that the analog-circuit-domain cancellation behaves best over "sufficiently narrowband" systems. Thus, analog-circuit-domain cancellation is limited by analog signal processing imperfections and bandwidth. To minimize the effects of the limitations in both the analog-circuit and digital domains, performing as much SIS as possible in the propagation domain is best.

2.3.3 Propagation-Domain SIS

The propagation domain consists of the antenna(s) and the propagation of electromagnetic (EM) waves. The benefit of SIS in this domain is that the self-interference is suppressed *before* it is a problem in the analog and digital circuitry. In antenna terminology, the suppression achieved in this domain is the magnitude of the S_{21} scattering parameter.

IBFD isolation techniques in the propagation domain include physical separation [29],

polarization diversity [29,42,47,48], via-suppression [49–51], tunable resonators [38,39,52], meta-materials [53–55], and circulators [17,56]. Cancellation techniques involve placing antennas in geometric configurations whereby the TX signal destructively interferes with itself creating a "spatial notch" at the location of the RX antenna(s) [20,29,37,40,41,57–59].

The following sections describe how each technique is accomplished and present how effective other researchers have demonstrated these methods to be. The specifications of interest are the achievable SIS, the fractional bandwidth, the amount of physical space required, and the number of elements required. Elements include each antenna, via, resonator, and meta-surface. Having fewer elements simplifies the design and lowers the fabrication cost and complexity.

Physical-Separation Isolation

Physically separating the TX and RX antennas is the most intuitive way to isolate them [29]. Physical separation is the isolation technique used in bi- and multi-static radar [28,60].

The Friis transmission equation [13], given by

$$P_r = \frac{P_{\mathrm{avg}} G_t G_r \lambda^2}{(4\pi R)^2}, \tag{2.4}$$

where:

$R =$ distance between antennas [m],

demonstrates that EM waves attenuate by R^2 as they propagate. As R increases, the achievable SIS increases quadratically. As long as $R \gg \lambda$ the SIS covers a large bandwidth. This isolation method only requires two elements: the TX and RX antennas. The space this method fills can be greater than tens of kilometers.

Polarization-Diversity Isolation

The polarization of an antenna describes the direction of the time-varying electric-field vector [13]. The applicable polarizations to this discussion are vertically linear, horizontally linear, right-hand circular (RHCP), and left-hand circular (LHCP) (see Figure 2.3).

(a) Vertical

(b) Horizontal

(c) RHCP, traveling out of page

(d) LHCP, traveling out of page
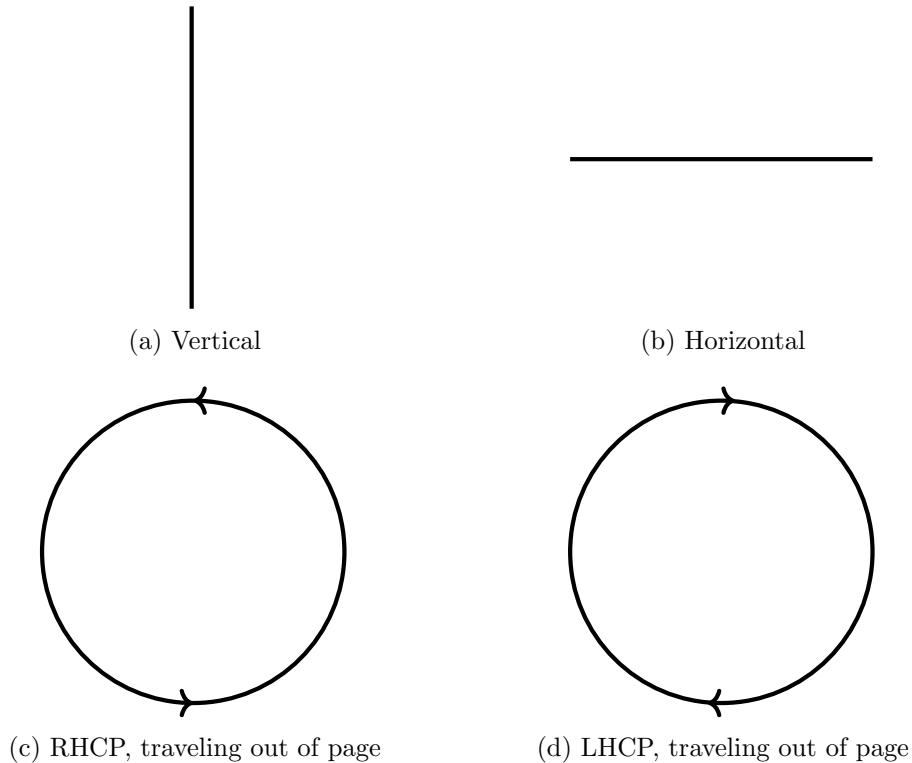
Fig. 2.3: Basic types of antenna polarizations.

A vertically polarized wave is better received with a vertically polarized antenna than with a horizontally polarized antenna. The same is true for RHCP and LHCP. Balanis [13] quantifies this concept by including a polarization mismatch term in the expression of the radar equation to account for antenna misalignment or diversity.

From EM boundary conditions, linearly polarized waves will reflect from a metallic surface with the same polarization, but circularly polarized waves switch the direction of polarization at each reflection (see Figure 2.4) [22].
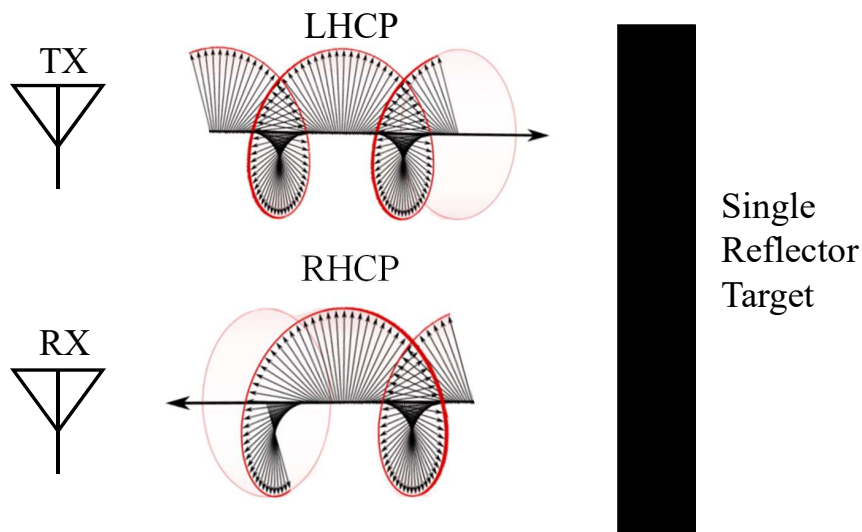
Fig. 2.4: Transmitting and receiving opposite circular polarizations.

For a single or an odd number of reflections, LHCP reflects to be RHCP and vice versa. A radar with two antennas can take advantage of this polarization diversity. For example, if the TX antenna is LHCP an RHCP RX antenna would receive the reflected waves with minimal mismatch. The polarization diversity increases isolation between TX and RX antennas without weakening the return signal by having a polarization mismatch. It has been shown that polarization diversity provides 30-40 dB of isolation over a 30-50% fractional bandwidth [42, 47, 48, 61]. Polarization diversity does not require more elements than the TX and RX antennas. The antennas can be spaced as close as 0.25λ [47].

Circular-polarization diversity is a common technique in radar meteorology to suppress rain clutter [61–63] and sense precipitation [64–66]. Rain-clutter suppression comes by using antennas with the same circular polarization. The EM waves reflect off raindrops once and switch polarization. The target has many surfaces so some of the reflections bounce an even number of times and remain the same polarization. The rain clutter is then cross-polarized while the target has some cross-polarization and some co-polarization returns.

Via-Suppression Isolation

Via-suppression isolation incorporates microstrip vias between the TX and RX antennas. These vias improve isolation by about 4 dB by shorting the surface waves before they couple with the other antenna [49]. The drawback to this method is the limited fractional bandwidth, 1%, over which the isolation is achievable [50]. Each via placed between or around the antenna adds more elements to the design. Kim and Yook [50] and Sarrazin et al. [49] have dozens of vias in their designs. The spacing between Sarrazin et al.'s antennas is less than 0.5λ.

Tunable-Resonator Isolation

Like the via-suppression technique, tunable resonators are another parasitic element that can be placed between antennas to reduce coupling. Wegener and Chappell [38,39] have shown that 20 dB of isolation is achievable, but is limited to a narrow fractional bandwidth, 0.3%. Wegerner and Chappell's design places one to four resonators between the antennas. Each resonator is made of several varactors, resistors, and dozens of vias. The antennas are placed 0.5λ apart.

Meta-Material Isolation

Similar to the via and resonator methods, meta-material isolation techniques involve placing a material or combination of materials designed for specific absorption or reflection properties between antennas. This meta-material suppresses surface waves from coupling with other antenna elements. 10-20 dB of isolation has been achieved over fractional bandwidths of 4% and 15% [53–55]. The meta-material design in [53] implements dozens of patch and via elements within a region 0.75λ wide.

Ferrite Circulator

For mono-static radar systems, the other suppression techniques described in Section 2.3.3 are not realizable because they require separate antennas for TX and RX. Instead, mono-static radars isolate the TX and RX with a nonreciprocal ferrite circulator. Circulators are included as a propagation domain SIS method (instead of a analog-circuit domain method) because the circulator replaces the other propagation domain SIS methods for a mono-static radar and can be combined with the analog-circuit domain SIS techniques described in Section 2.3.2.

A circulator is a three-port device that allows power to flow between ports in only one direction. Figure 2.5 shows an imperfect circulator where power is designed to flow from port 1 to port 2, port 2 to port 3, and port 3 to port 1.
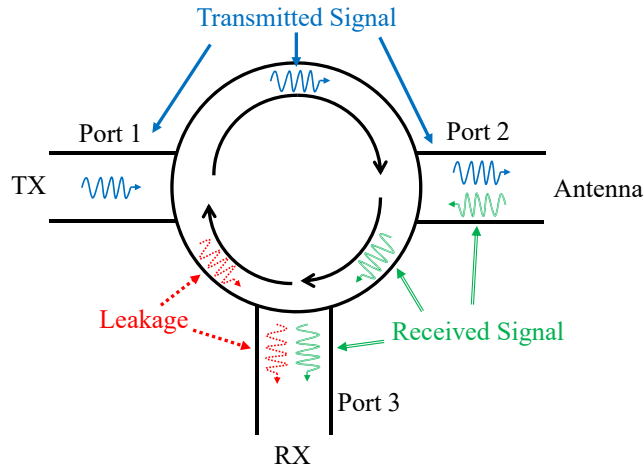
Fig. 2.5: Mono-static radar application of a ferrite circulator.

Ideally, the isolation from port 1 to port 3 is infinite, meaning the TX and RX are completely isolated. However, small mismatches at the ports and lossy transmission lines result in a finite isolation [67]. In practice, circulators provide 30 dB isolation at best [17,56]. The fractional bandwidth of a ferrite cirulator can be as high as 36% [68]. A circulator interfaces with only one antenna so the number of elements and physical space this isolation method requires is small.

Spatial-Notch Cancellation

A spatial notch is a null in the antenna radiation pattern and is created when transmitted EM waves destructively interfere with each other. This cancellation is formed by EM waves lining up out of phase. Placing the RX antenna in this null isolates it from the TX antennas.

Phase diversity can be induced by spacing two TX antennas such that one is half a wavelength further away from the RX antenna than the other TX antenna [34], or the TX antennas can be equally spaced but fed with different phases [57, 58]. Research shows a wide range of achievable suppression, 20-55 dB. The disadvantage of this method of suppression is the number of antennas and physical space required to create the geometry needed. Additionally, since the location of the notch is dependent on the frequency of the transmitted EM wave, the bandwidth of cancellation is narrow. Kolodziej et al.'s [58] design uses nine antennas in a circular region with a diameter of 0.5λ and only achieves a 4% fractional bandwidth.

Some research has been done to widen the fractional bandwidth to 25% and 50% of the spatial notch configuration at the expense of larger and more complicated geometries [40,41].

2.4   RainCube

The only realized CubeSat-borne radar to date is the NASA JPL's Radar in a CubeSat (RainCube) [3]. Launched in 2018, the RainCube was a 6U CubeSat that implemented a Ka-band radar to observe weather conditions on Earth. Operating at 35.75 GHz with a 20 MHz bandwidth, the RainCube implemented PDW radar with 10 W peak power and a 10% duty cycle. From (2.2), this corresponds to transmitting an average power of 1 W. The RainCube had a deployable, mesh-parabolic dish antenna. The antenna weighed approximately 0.5 kg and occupied a 1.5U volume when stowed [4].

CHAPTER 3

RESEARCH AND DESIGN DECISIONS

This chapter presents how the current research builds on the principles explored in Chapter 2 to decide the approach to meet each objective declared in Chapter 1. Decisions about the radar type, suppression type, platform size, and operating frequency are presented. Chapters 4–6 present the methods and results of each objective.

3.1 Radar Type

The five types of radar presented in Section 2.2 are classified into two subgroups: pulse and continuous. The decision matrix represented in Table 3.1 demonstrates why the continuous group is a more advantageous type of radar. The criteria used to compare the subgroups are the average power output, the radar's ability to process multiple modes, the impact on the battery, resistance to EW jamming techniques, the number of nodes formed in a constellation, and the amount of SIS required. Criteria are ranked 0-3 with 3 being the best.

Table 3.1: Comparison of radar subgroups.

Subgroup	P_{avg}	Modes	Power Supply	EW	Nodes	SIS	Total
Pulse	1	1	1	0	2	3	8
Continuous	3	2	2	1	3	0	**11**

Table 3.1 demonstrates that the continuous type of radar, which includes CW and FMCW, is desirable. The advantages the continuous group provides in average power output, multiple processing modes, low deterioration of power supply, EW protection, and extra multi-static nodes drives the search to find ways to produce adequate SIS to realize CW or FMCW radar on a small platform.

Since FMCW provides range information in addition to the other CW capabilities, an FMCW signal is better for a CubeSat-borne radar. This permits the radar to better identify the locations of space vehicles, debris, and asteroids. Since the focus of this work is SIS, the tests in Chapters 4–6 are simplified and verified with a single-frequency CW signal. These test remain valid for any frequency within the bandwidth of the antennas and front-end components; thereby, the tests also verify FMCW radar capabilities.

3.2 Suppression Type

The SIS methods presented in Section 2.3.3 are compared in a decision matrix shown in Table 3.2. The fractional bandwidth is represented by Δ. The criteria used to compare methods are quantified and ranked 0-3 with 3 being the best. Since Section 3.1 selects continuous radar, the suppression method must have at least 2 antennas to support continuous radar (see Section 2.2.4). Thus, while the circulator has the fewest elements, it receives a 0 rank in the decision matrix because it only uses one antenna which cannot support continuous radar.

Table 3.2: Comparison of SIS techniques.

Method	SIS	Δ	Elements	Physical Space	Total
Separation	3	3	2	0	**8**
Polarization	2	3	2	2	**9**
Via	0	0	1	2	3
Resonator	1	0	1	2	4
Meta-material	1	1	1	2	5
Circulator	2	2	0	2	6
Spatial Notch	2	2	1	2	7

The comparison in Table 3.2 demonstrates that physical separation and polarization diversity are the most promising SIS techniques. The amount of achievable physical sep-

aration on a small platform is limited. Unlike the rain-clutter suppression explained in Section 2.3.3, it is assumed that the target is a single reflector like a flat plate. This allows for the radar return to have the opposite polarization as the transmit signal, creating the required polarization diversity.

3.3 Platform Size

The RainCube represents a basis for platform size and power, allowing the capabilities of the CW radar to be compared to those of the RainCube (see Section 2.4). Thus, this thesis develops a 6U CubeSat with a 1 W average transmitted power.

3.4 Operating Frequency

The main distinction between the RainCube and the CW radar design is the operating frequency. The antennas for the CW radar are designed to operate at 2.4 GHz. This makes fabrication feasible with equipment found at Utah State University's laboratories. Additionally, RF components that operate at 2.4 GHz are more readily available.

Antennas designed and verified at 2.4 GHz can later be scaled to operate equivalently at other frequencies.

CHAPTER 4

DESIGN METHODS AND RESULTS: SELF-INTERFERENCE SUPPRESSION

Objective 1 of this thesis is to explore how much SIS is achievable by combining physical-separation and polarization-diversity techniques on a limited platform size. This chapter describes a design that incorporates decisions in Chapter 3 and presents simulation and fabrication results to meet Objective 1.

4.1 Noise and Suppression

Before designing and simulating circularly polarized antennas, it is important to determine how much suppression is required for a radar system carried by a 6U CubeSat. This understanding establishes a benchmark against which to evaluate the antennas during testing. This section introduces the derivation of the noise power in a radar RX and identifies how much isolation is required between the antennas.

4.1.1 Receiver Noise Floor

The noise in an RX is defined in decibels (dB) as

$$N = 10 \log_{10}(k T_{\text{sys}} B_n), \tag{4.1}$$

where:

$N =$ Noise power [dB]

$k =$ Boltzmann constant $1.38 \ 10^{-23}$ [Joules/K]

$T_{\text{sys}} =$ Effective system temperature [K]

$B_n =$ Effective bandwidth [Hz].

The effective system temperature, T_{sys}, is the superposition of the effective temperature of each RX sub-component [69],

$$T_{\text{sys}} = T_A + T_R + T_{AL} + T_{LL}, \tag{4.2}$$

where:

T_A = Antenna noise temperature

T_R = Effective receiver temperature

T_{AL} = Antenna loss temperature

T_{LL} = Transmission line noise temperature.

The antenna noise temperature can be approximated according to where the antenna is pointing. A CubeSat-borne, directional antenna in low-Earth-orbit that looks toward the Earth with low minor lobes approximate $T_A \approx 290$ K, the temperature of the Earth. An antenna with stronger minor lobes that point at space or an antenna whose main lobe points away from the Earth decrease the antenna noise temperature, making 290 K a conservative approximation.

As derived by Doerry [70], the effective receiver noise temperature is

$$T_R = T_1 + \frac{T_2}{G_1} \tag{4.3}$$

$$= T_0(F - 1), \tag{4.4}$$

where:

T_1 = Temperature of 1st RF component [K]

T_2 = Temperature of 2nd RF component [K]

G_1 = Gain of 1st RF component

T_0 = Reference temperature [K] (290 K in LEO)

F = Receiver noise factor.

The noise factor is the ratio of the input and output SNRs of the RX. The noise factor for a RX is expressed as

$$F = F_1 + \frac{F_2 - 1}{G_1} + \frac{F_3 - 1}{G_1 G_2} + ... + \frac{F_k - 1}{G_1 G_2 ... G_{k-1}}, \tag{4.5}$$

where:

F_1, F_2, F_3, F_k = Noise factor of 1st, 2nd, 3rd, kth RF component respectively

G_1, G_2, G_k = Gain of 1st, 2nd, kth RF component respectively.

The first RF component is typically a band-pass filter (BPF) followed by a low-noise amplifier (LNA). The BPF prevents out-of-band frequencies from damaging the LNA. The LNA typically has a large gain (≥ 20 dB) so (4.5) is typically truncated to the first two terms

$$F = F_1 + \frac{F_2 - 1}{G_1}. \tag{4.6}$$

The noise figure is the noise factor expressed in dB. The noise figure is a common specification on a datasheet for an active component. The noise figure for a passive component is the magnitude of the insertion loss.

Taking the pass-band insertion loss of the BPF to be 1.5 dB, the LNA gain to be 20 dB, and the LNA noise figure to be 2 dB (typical values), the effective receiver temperature can be calculated from (4.4)

$$\begin{aligned} T_R &= T_0(F_1 + \frac{F_2 - 1}{G_1} - 1) \\ &= 290(1.41 + \frac{1.58 - 1}{0.71} - 1) \\ &\approx 360 \text{K}. \end{aligned}$$

The antenna loss temperature is defined as

$$T_{AL} = \left(\frac{1}{e_A} - 1 \right) T_{PA}, \tag{4.7}$$

where:

e_A = Antenna efficiency

T_{PA} = Antenna physical temperature.

Assuming an antenna with low loss resistance, $e_A \approx 1$ and $T_{AL} = 0$.

The equation for the transmission line loss temperature is of the same form. Assuming efficient transmission lines, $T_{LL} = 0$.

The conservative approximations for T_A and T_R make up for the assumptions that the antenna and transmission lines are lossless. Combining the derived values for T_A, T_R, T_{AL}, and T_{LL} results in

$$T_{\text{sys}} \approx T_A + T_R$$

$$\approx 290 + 360$$

$$\approx 650 \text{ K}.$$

Assuming the antennas have a 2.5% fractional bandwidth, the effective receiver bandwidth is 60 MHz. To account for imperfections in the antennas, 65 MHz is applied to this calculation.

The noise power is then

$$N = 10 \log_{10}(k T_{\text{sys}} B_{eff})$$

$$= 10 \log_{10}(k \cdot 650 \cdot 65 \times 10^6)$$

$$= -123 \text{ dBW}.$$

Commonly, radar power is expressed in decibels relative to 1 mW (dBm). Power in dBm is 30 dB greater than power relative to 1 W (dBW). So, $N = -93$ dBm.

4.1.2 Suppression Requirement

For the self-interference to have a negligible impact on the RX it must be suppressed to, or below, the RX's noise floor (see Figure 4.1). Mathematically, that is

$$S \geq P_{\mathrm{avg}} - N \text{ (dB)}, \tag{4.8}$$

where:

$S =$ Total SIS in RX [dB].

By choosing the P_{avg}, the total suppression required can be calculated. To stay comparable to the RainCube (see Section 3.3), the P_{avg} in this model is 1 W (30 dBm). The total SIS in the RX can additionally be split into the superposition of the suppression in each domain. Applying typical values from the literature for the suppression in the digital and analog domains (see Section 2.3), and assuming a 54 dB dynamic range, (4.8) becomes

$$S \geq P_{\mathrm{avg}} - N \text{ (dB)}$$
$$|S_{21}| + S_a + S_d \geq 30 - (-93) \text{ (dB)}$$
$$|S_{21}| + 30 + 54 \geq 123 \text{ (dB)}$$
$$|S_{21}| \geq 39 \text{ (dB)}, \tag{4.9}$$

where:

$|S_{21}| =$ Propagation-domain suppression (i.e. insertion loss) [dB]

$S_a =$ Analog-circuit-domain suppression [dB]

$S_d =$ Digital-domain suppression [dB].
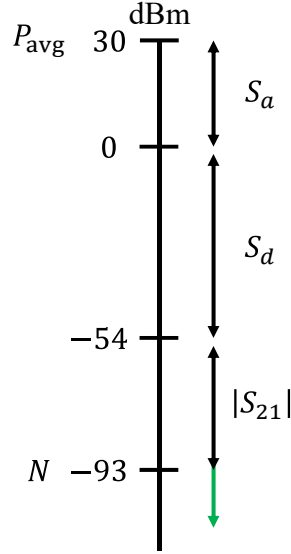
Fig. 4.1: Visualization of suppressing the self-interference below the noise floor.

Figure 4.1 presents the manner by which the three domains of suppression push the self-interference below the RX's noise floor. The derivation leading to (4.9) shows the goal of this research. By implementing physical separation and polarization diversity techniques, the $|S_{21}|$ of the CW radar must be greater than 39 dB.

4.2 Antenna Simulation Results

This section presents results of antenna models designed using Ansys HFSS$^{®}$ to meet the suppression requirements developed by Section 4.1. To improve on the RainCube, the presented antennas are low-profile patch antennas that are implemented on the solar panels. This reduces the volume dedicated to the antenna and removes the need for deployment. As explained in Section 3.4, the antennas are designed to operate at 2.4 GHz.

To realize polarization diversity, one antenna is LHCP and the other is RHCP. Figure 4.2 shows two circularly polarized patches that are designed using the corner-cut technique.
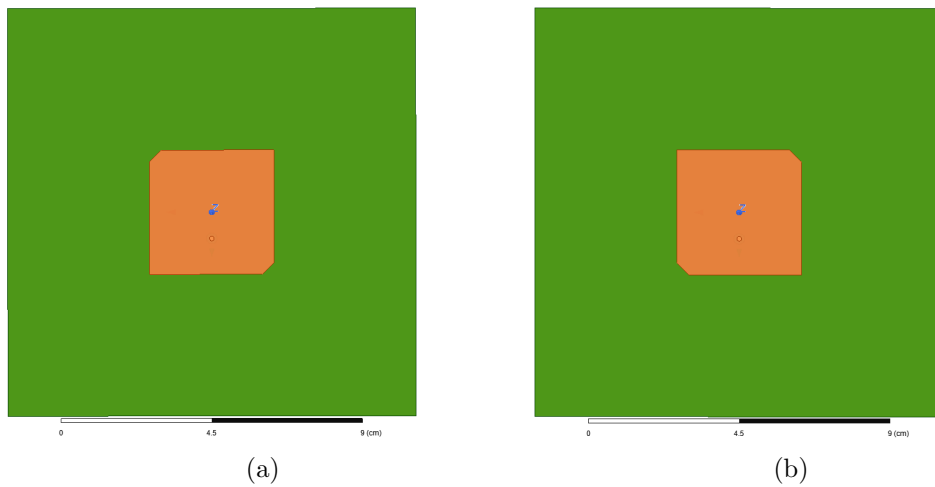
Fig. 4.2: LHCP (a) and RHCP (b) patch antennas designed using the corner-cut method.

The patches shown in Figure 4.2 are designed on a Rogers Corporation substrate. The patches are about 0.3λ in each direction. The corners are trimmed about 0.03λ along each side. Appendix A specifies the substrate's material properties, how to make a circularly polarized antenna using the corner-cut method, and the precise geometry of the final design depicted in Figure 4.2.

4.2.1 Simulated Antenna Performance

The antennas depicted in Figure 4.2 are designed such that the simulation results demonstrate acceptable radiation requirements ($S_{11} < -10$ dB) and axial ratio (< 3 dB). The results for the LHCP antenna are shown in Figures 4.3 and 4.4. Figure 4.5 shows the elevation pattern of the LHCP antenna. The RHCP results for S_{11}, axial ratio, and elevation pattern are equivalent.
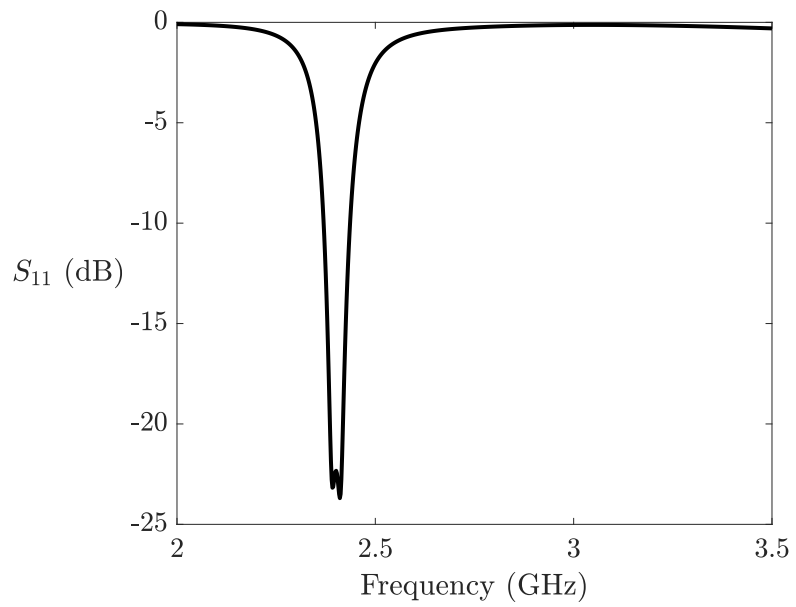
Fig. 4.3: Simulated LHCP return loss.
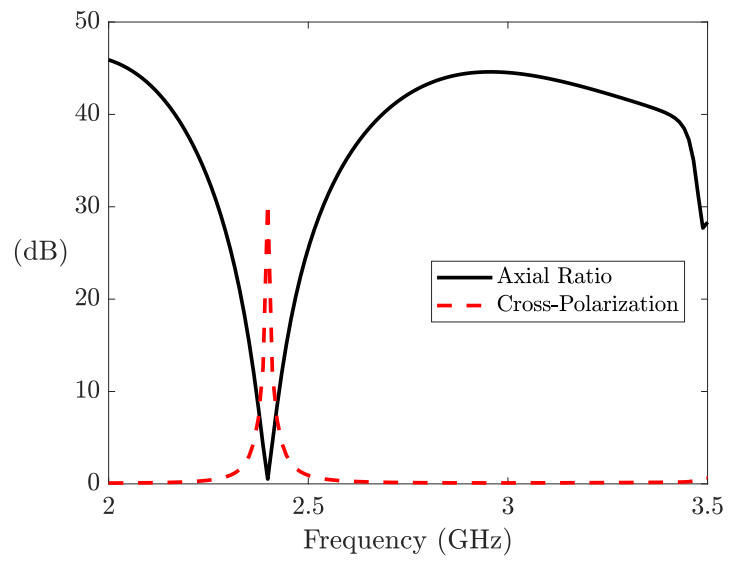
Fig. 4.4: Simulated LHCP axial ratio and cross-polarization.
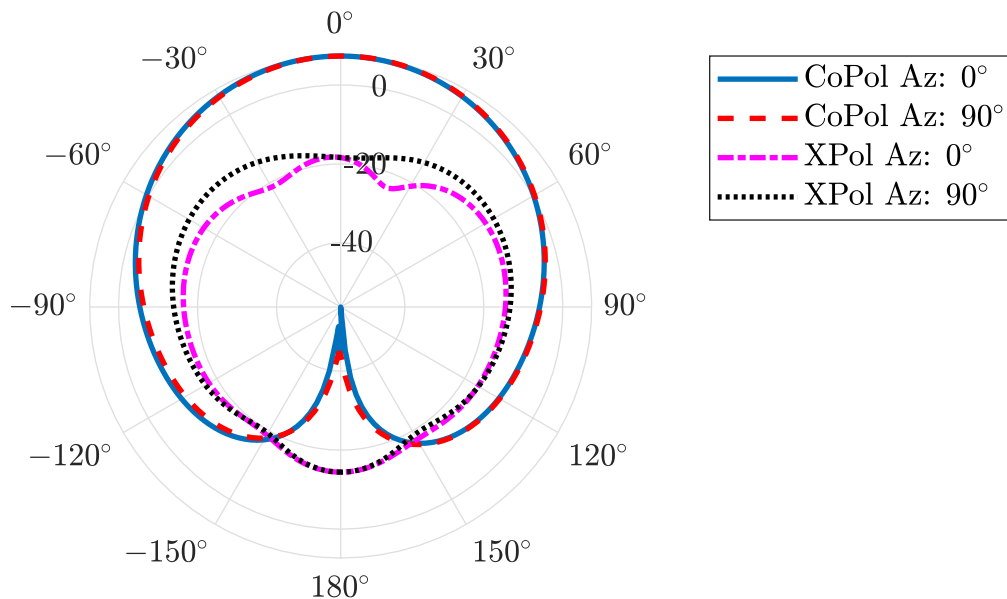
Fig. 4.5: Elevation pattern of LHCP patch antenna.

In addition to the axial ratio, Figure 4.4 shows the cross-polarization of the LHCP antenna. Cross-polarization is the difference between the co-polarization (CoPol) and cross-polarization (XPol) radiation levels. The cross-polarization of the LHCP antenna is near 30 dB. Figure 4.5 shows the radiation levels of CoPol and XPol vs elevation angle through two cuts in azimuth (Az) angle. Near bore-sight, the CoPol gain is 7.3 dB and the cross-polarization is more than 27 dB down, which is congruent with Figure 4.4.

4.2.2 Simulated Antenna Isolation

To simulate the isolation between the antennas, two configurations are modeled. The first is with the antennas "looking up" when mounted on the inside of the solar panels (Figure 4.6b). The second is "looking down" when mounted on the outside of the panels (Figure 4.6c). The S_{21} simulation results are shown in Figure 4.7.
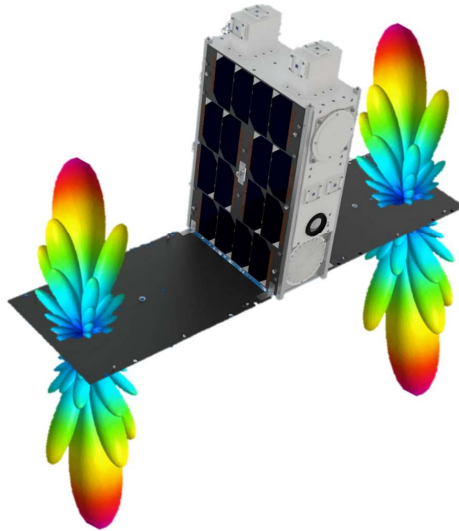
(a) Look-up and look-down configurations.
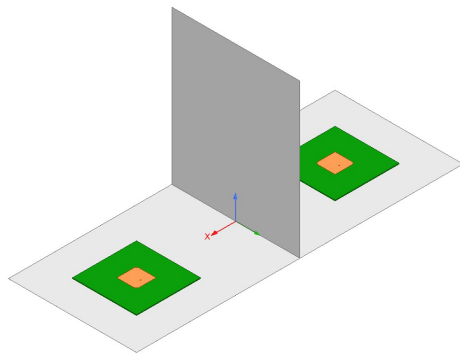
(b) Model of look-up configuration.
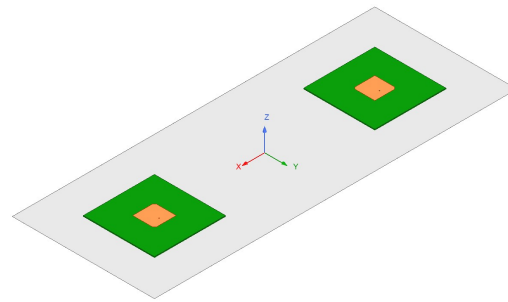
(c) Model of look-down configuration.

Fig. 4.6: Look-up and look-down simulation models.
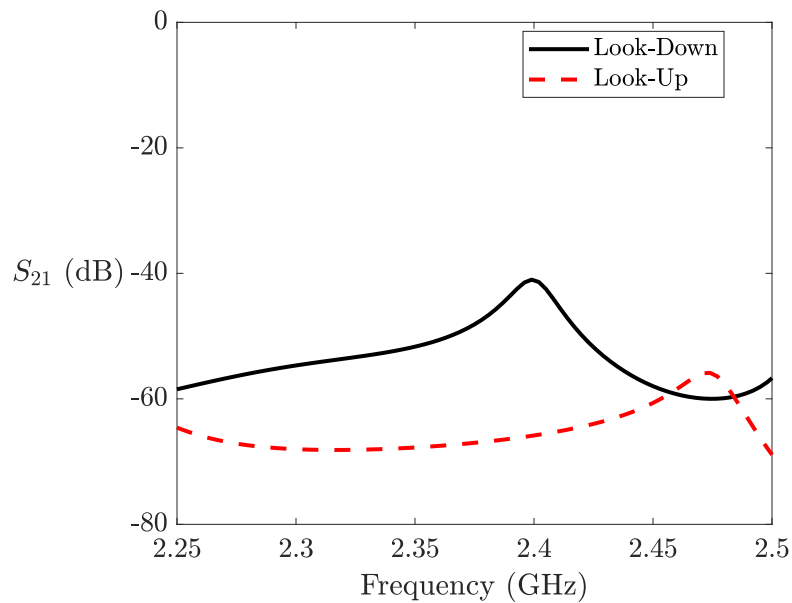
Fig. 4.7: Simulated S_{21} of look-up and look-down configurations.

At 2.4 GHz, there is 41 dB of isolation when looking down and 65 dB when looking up. These results give confidence that the 39 dB of isolation required by (4.9) can be realized.

4.3   Antenna Prototype Results

This section provides the results of fabricating and testing the prototype antennas. The patch antennas are fabricated using an LPKF ProtoMat® S103 milling machine. Figure 4.8 shows the fabricated antennas after connectors have been mounted.
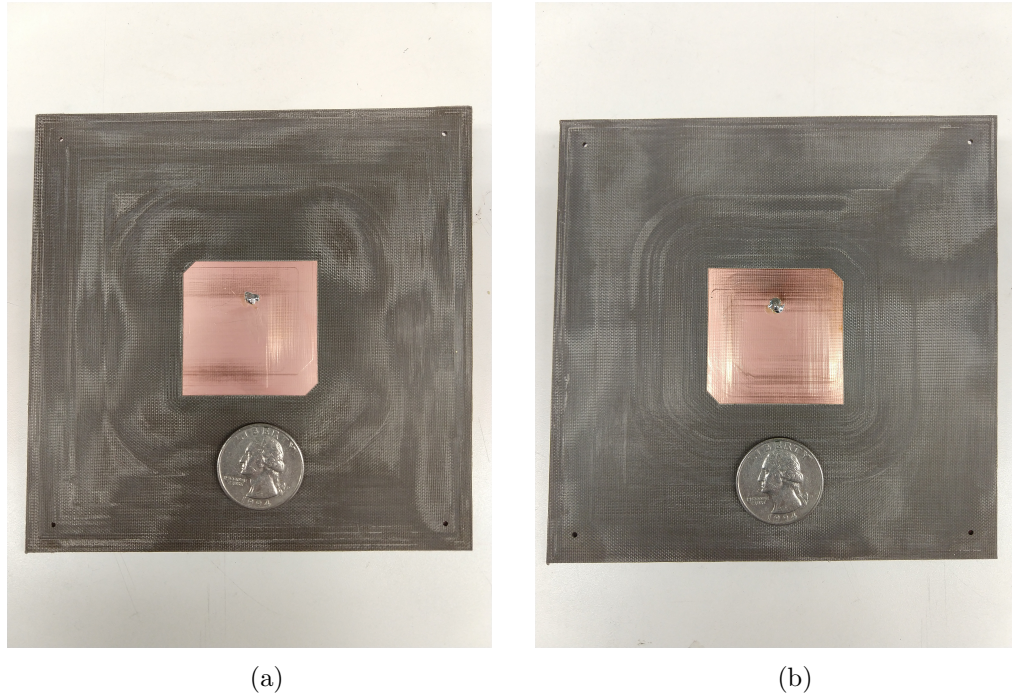
Fig. 4.8: Fabricated LHCP (a) and RHCP (b) patch antennas.

Tests are performed to verify that the antenna prototypes behave as designed. The first type of test verifies the individual antenna performance. The second type of test measures the isolation between antennas on a CubeSat model. In both test types, an Agilent Technologies FieldFox N9914A network analyzer performs the measurements.

4.3.1 Prototype Antenna Performance

Measurements of the return loss of the fabricated antennas are shown in Figure 4.9. These results show that the LHCP S_{11} is comparable to the simulation results, but there is minor degradation in the RHCP antenna. The discrepancy can be attributed to milling tolerances. The RHCP S_{11} curve shows the null is slightly higher in frequency than desired. This suggests the patch is slightly smaller than designed. This change in geometry also impacted the antenna's return loss, though not significantly; S_{11} below -15 dB is still acceptable.
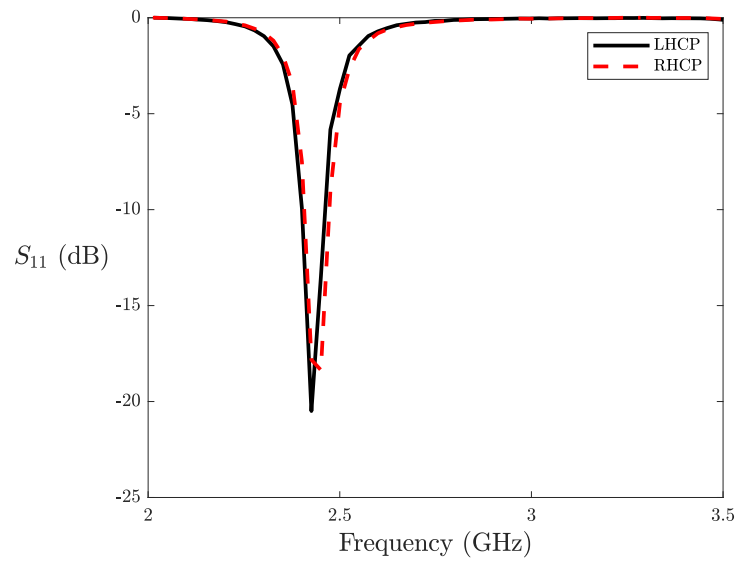
Fig. 4.9: Return loss of fabricated patch antennas.

Two tests verify the circular polarization of the antennas. The test set-up for the first test is shown in Figure 4.10.
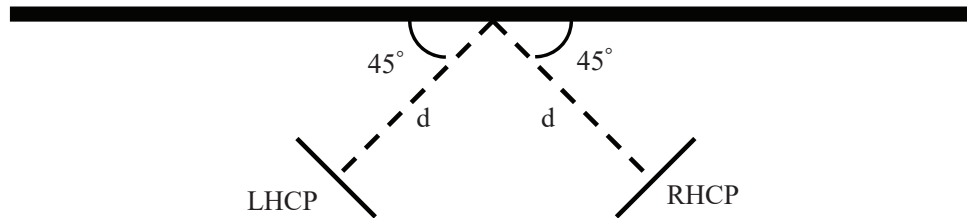
Fig. 4.10: Test set-up to verify circular polarization.

The network analyzer measures the S_{21} parameter while the antennas are fixed at $45°$ angles from a flat, metallic surface. Then, one of the antennas is rotated $90°$ about the axis normal to the patch (depicted with a dashed line) and the measurement is taken again. Figure 4.11 overlays the measurements. Since the orthogonal measurements closely match each other near 2.4 GHz, the test shows that the transmission between antennas is not dependent on the relative rotational orientation of the antennas. This independence verifies that the antennas are circularly polarized near 2.4 GHz.
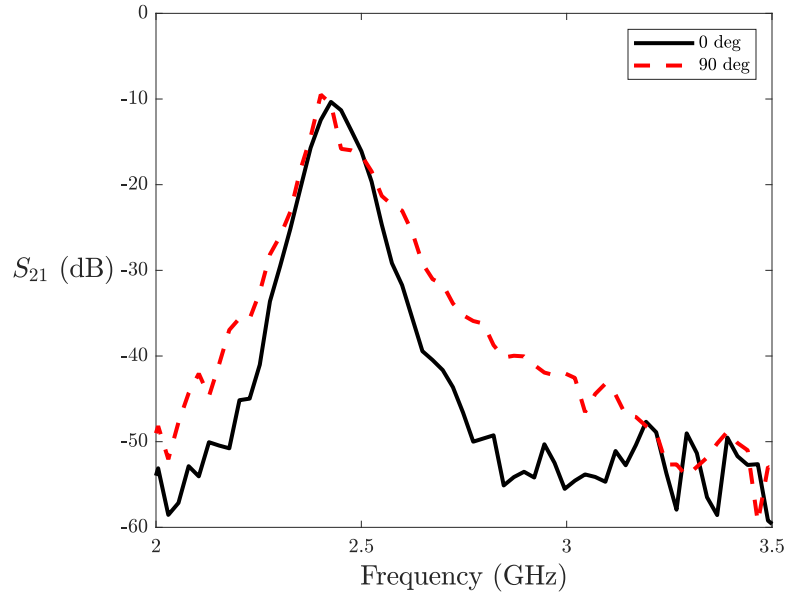
Fig. 4.11: Measured S_{21} between antennas in two different orientations.

The second test quantitatively verifies the opposite circular polarization of the antennas by measuring the cross-polarization level. First, the set-up in Figure 4.10 is used to measure the received power for the CoPol. Then, the antennas are spaced a distance of $2d$ and pointed directly at each other to measure the XPol (see Figure 4.12). The cross-polarization is the difference of these measurements. Table 4.1 shows the received power for CoPol and XPol when the transmitted power is 0 dBm and $d = 32.4$ cm. The receive power measurement is taken multiple times and averaged to better estimate the cross-polarization.
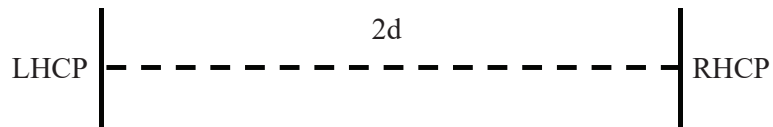
Fig. 4.12: Test set-up to measure XPol level of fabricated antennas.

Table 4.1: Measurements of CoPol and XPol power levels of fabricated antennas.

Polarization	Received Power (dBm)				Average Power (dBm)
CoPol	-22	-24	-23	-22	-23.25
XPol	-42	-38	-42	-43	-41.25

From Table 4.1, the difference between the average CoPol and XPol is 18 dB. 18 dB of cross-polarization is lower than the 27 dB predicted by simulation. Part of this discrepancy is due to the fact that this test could not be performed in the anechoic chamber. This results in the interference of waves reflecting from the walls and other surfaces in the room. Noting this measurement inaccuracy, 18 dB of cross-polarization is still acceptable to verify that the antennas are opposite circularly polarized.

The test set-up in Figure 4.10 also provides the ability to calculate the gain of the antennas using the Friis transmission equation (2.4). Rearranging (2.4) gives

$$\frac{P_r}{P_{\text{avg}}} = \frac{G_t G_r \lambda^2}{(4\pi R)^2}. \tag{4.10}$$

The LHCP antenna is at the TX and the RHCP at the RX. The ratio

$$\frac{P_r}{P_{\text{avg}}}$$

is the S_{21} parameter measured on the network analyzer as shown in Figure 4.11. (4.10) can be rearranged so that

$$G_t G_r = S_{21} \frac{(4\pi R)^2}{\lambda^2}. \tag{4.11}$$

Or, in dB,

$$G_t + G_r = S_{21} + 10 \log \left(\frac{[4\pi R]^2}{\lambda^2} \right) \text{(dB)}. \tag{4.12}$$

Table 4.2 provides the values measured for R and S_{21} and calculated for $G_t + G_r$ at 2.4 GHz.

Table 4.2: Calculation gain of prototype antennas.

Parameter	Value
R	14 cm
λ	12.5 cm
S_{21}	-10 dB
$G_t + G_r$	13 dB

Assuming the LHCP and RHCP antennas have the same gain, the gain of each antenna is 6.5 dB. This is lower than the 7.3 dB estimated in simulation, but still acceptable for a patch antenna.

4.3.2 Prototype Antenna Isolation

A CubeSat model made out of aluminum foil holds the prototype antennas during testing. This section discusses the practicality of this model compared to a metallic frame and presents the test results from using the CubeSat model.

Practicality of an Aluminum-Foil Model

An aluminum-foil model (see Figure 4.13) adequately replaces a typical CubeSat metallic frame because the thickness of aluminum foil is much larger than the skin depth of aluminum at 2.4 GHz.
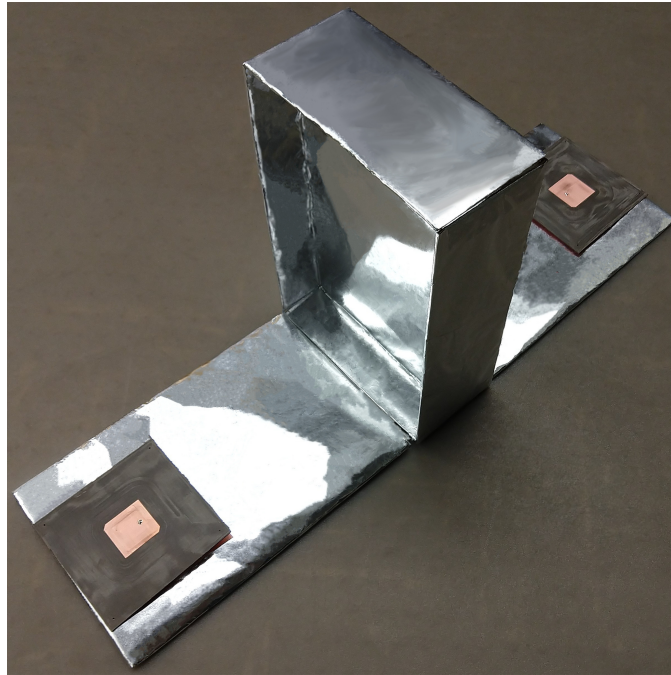
Fig. 4.13: CubeSat model made from aluminum foil.

Skin depth, δ_s, characterizes the depth in meters an EM wave can penetrate a conductive medium. The thicker or more conductive a conductor is, the less an EM wave can pass through it. The magnitude of an EM wave penetrating a conductor is less than 1% of its initial value at a depth of $5\delta_s$. The formula for skin depth, given by Ulaby [71], is

$$\delta_s = \frac{1}{\sqrt{\pi f \mu \sigma_c}},$$ (4.13)

where:

f = Frequency [Hz]

μ = Magnetic permeability [H/m]

σ_c = Conductivity [S/m].

At 2.4 GHz, the skin depth of aluminum ($\sigma_c = 3.5 \times 10^7, \mu = 4\pi \times 10^{-7}$) is

$$\delta_s = \frac{1}{\sqrt{\pi(2.4 \times 10^9)(4\pi \times 10^{-7})(3.5 \times 10^7)}}$$
$$= 1.74 \times 10^{-6} \text{ m.}$$

This CubeSat model uses aluminum foil that is 0.02 mm thick, which is 11.5 times larger than the skin depth. Only a negligible amount of energy passes through the aluminum foil. Since the aluminum foil is thick enough to block EM waves, the foil is an adequate substitute for an actual CubeSat frame when testing the isolation capabilities of the structure.

Isolation Results Using CubeSat Model

Measurements of S_{21} with the CubeSat prototype verify the simulation results of Section 4.2.2. Figure 4.14 shows the test set-up for the S_{21} measurements in an anechoic chamber and Figure 4.15 provides the measured results.
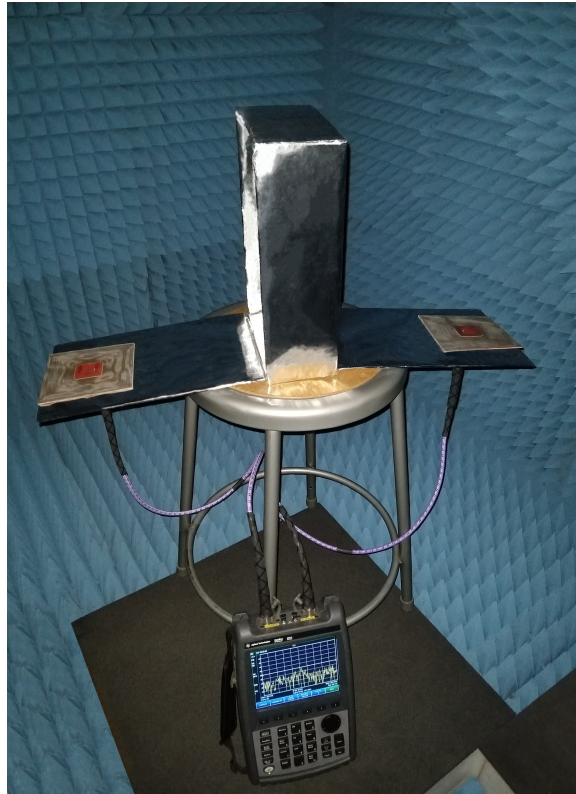
Fig. 4.14: Test set-up for measuring S_{21} in look-up configuration.
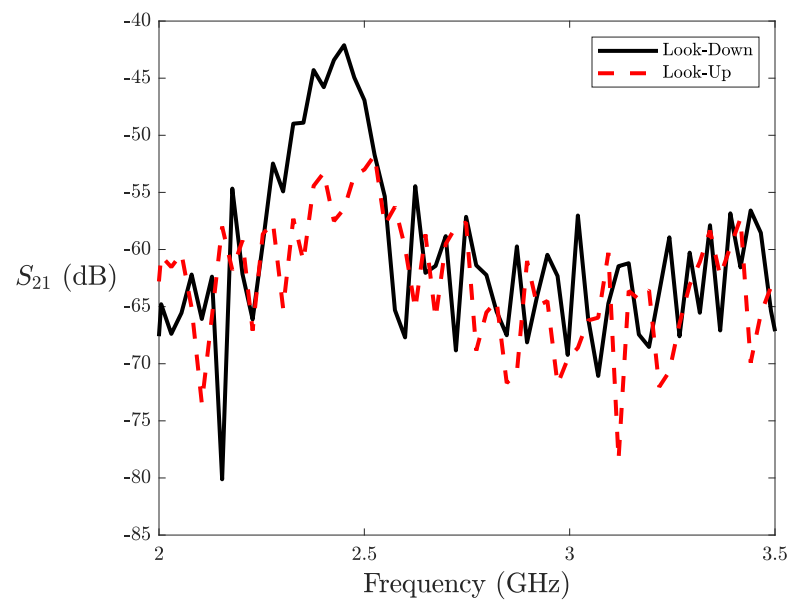
Fig. 4.15: S_{21} measurements in look-up and look-down configurations.

Figure 4.15 shows 43 dB of isolation when looking down and 57 dB when looking up. The measured isolation, when looking down, is comparable to simulation. When looking up, the measured isolation is 8 dB less than simulation. Though corresponding to a received power more than six times greater than the simulation shows, this discrepancy is not a concern when comparing the S_{21} values as unitless ratios and not in dB (see Table 4.3)

Table 4.3: Comparison of the simulated and measured S_{21} in look-up configuration.

S_{21}	dB	Unitless
Simulation	-65	3.16×10^{-7}
Measurement	-57	2.00×10^{-6}

The unitless S_{21} demonstrates that the power coupled from TX to RX is more than six orders of magnitude less than the transmitted power. With these small magnitudes of power, any noise present in the network analyzer has a noticeable effect on the measured power. Figure 4.15 shows that the noise floor of the network analyzer is not much further below the measured S_{21} (about -65 dB), suggesting that the noise could be tainting the measurement.

Even with the effects of noise, the measured isolation is greater than the amount required by (4.9). This verifies that the combination of physical separation and polarization diversity adequately suppresses the self-interference of CW radar. The additional suppression achieved in the look-up configuration demonstrates that the CW radar can be unaffected by self-interference even when the SIS realized in the digital and analog domains are lower than the values assumed in the derivation of (4.9).

Isolation vs Spacing

Another metric of interest is how close together the antennas can be placed without violating the minimum required isolation of 39 dB as derived in (4.9). This test is done in an anechoic chamber with the set-up shown in Figure 4.16. This test was performed five times and averaged for each spacing. Table 4.4 shows the measured and averaged S_{21} for each spacing, D.
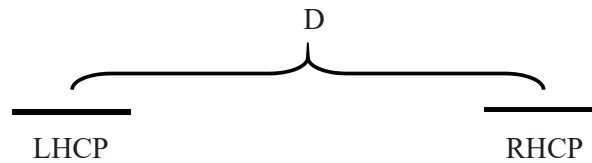
Fig. 4.16: Test set-up for measuring the S_{21} for different spacing, D.

Table 4.4: Measured S_{21} with different spacing.

Spacing (mm)	Spacing (λ)	S_{21} (dB)					Average S_{21} (dB)
100	0.80	-32.2	-32.3	-32.4	-32.6	-32.7	-32.5
140	1.12	-36.4	-36.6	-36.6	-37.1	-36.7	-36.8
180	1.44	-39.9	-39.4	-39.5	-38.5	-38.6	-39.0
220	1.76	-41.7	-41.5	-42.1	-41.5	-40.4	-41.4
260	2.08	-42.7	-43.0	-42.0	-42.9	-43.5	-42.9
300	2.40	-44.9	-45.3	-44.6	-43.3	-45.0	-44.6
340	2.72	-46.2	-47.0	-48.3	-47.0	-46.5	-47.2
380	3.04	-46.7	-47.2	-48.0	-48.9	-47.6	-47.9
420	3.36	-48.8	-51.5	-48.9	-49.2	-50.1	-49.9
460	3.68	-48.3	-49.2	-49.1	-53.6	-51.2	-50.8
500	4.00	-51.6	-52.3	-52.0	-50.6	-51.4	-51.6
540	4.32	-50.2	-49.8	-53.3	-52.9	-53.5	-52.4
560	4.48	-53.4	-53.3	-51.1	-51.9	-52.5	-52.2

As expected from (4.10), the S_{21} in Table 4.4 decreases as the spacing increases. Since isolation is the inverse of S_{21}, the isolation increases as the spacing increases. Table 4.4 demonstrates that the spacing between antennas must be at least 1.44 λ to maintain the minimum isolation of 39 dB derived in (4.9).

CHAPTER 5

DESIGN METHODS AND RESULTS: ARRAY TRADE-OFF

Objective 2 of this thesis investigates the achievable isolation when patch-antenna arrays replace the single-patch antennas designed in Chapter 4. This chapter presents simulation models and results that accomplish Objective 2.

Antenna arrays are common since they increase the antenna's gain and decrease the effects of clutter in the received signal. Clutter is the radar return from objects seen by the minor lobes of the antenna pattern. The trade-off is that an array takes up more space than a single element.

Increasing the gain of the antenna pattern makes the antenna more directive. This suggests that the isolation between the TX and RX increases since the TX is not pointed at the RX. The reason for studying the effects of an array is that self-interference occurs between each element in both arrays. Since the distance between each pair of TX and RX array elements is not constant, the amount of coupling is different for each pair. The effect this has on self-interference is an important characteristic to understand to adequately suppress the interference.

5.1   Array Simulation Model

The array effects are modeled and observed in simulation only. The array structure is fed with a microstrip feed network and shown in Figure 5.1. The feed network is placed on the opposite side of the ground plane as to not distort the behavior of the antenna elements. The substrate and ground layers are transparent so the feed network and patch elements are simultaneously visible. Figure 5.2 shows the arrays integrated on the CubeSat model. The arrays are spaced so that their centers are 437.5 mm (3.5 λ) apart.
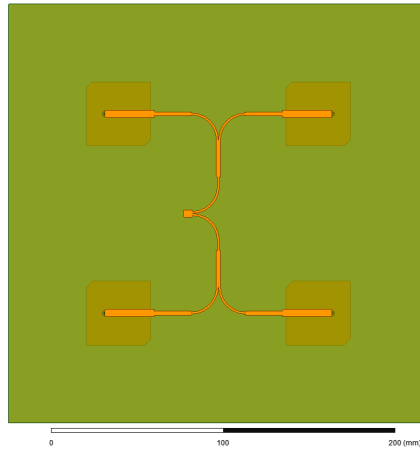
Fig. 5.1: LHCP array and feed network viewed from the bottom.
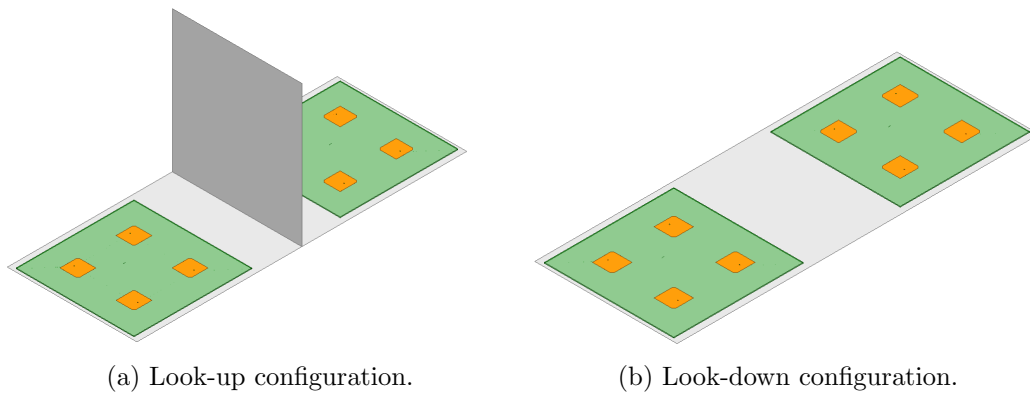
(a) Look-up configuration.

(b) Look-down configuration.

Fig. 5.2: Simulation models of antenna arrays.

To compensate for the larger size of the array, the CubeSat model is enlarged to keep the entire array on the solar panel. Realistically, the size of the CubeSat is fixed. The practical solution is to design an antenna array that operates at a higher frequency so all the elements fit within the size constraints of the CubeSat. To keep the results comparable to the single element simulations of Section 4.2, no changes in the geometry and frequency of individual patches are made.

5.2 Array Simulation Results

This section presents the results of simulations using the 2x2 antenna array model. The array performance and isolation simulations are described in the following two subsections.

5.2.1 Simulated Array Performance

As with the single-element antenna (see Section 4.2.1), the arrays are designed to demonstrate acceptable radiation characteristics and axial ratio. The simulated characteristics for the LHCP array are shown in Figures 5.3 and 5.4. Figure 5.5 shows the elevation pattern of the LHCP array. The RHCP-array results for S_{11}, axial ratio, and elevation pattern are equivalent.
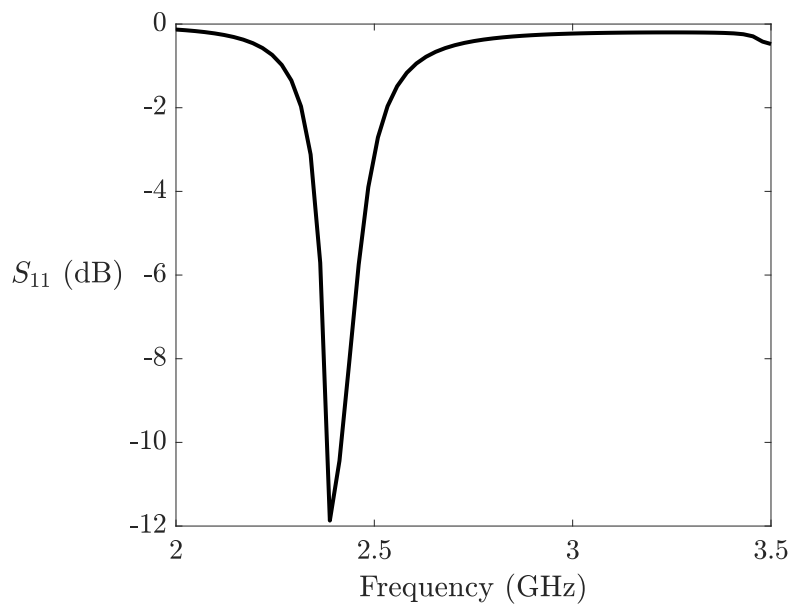
Fig. 5.3: Simulated LHCP-array return loss.
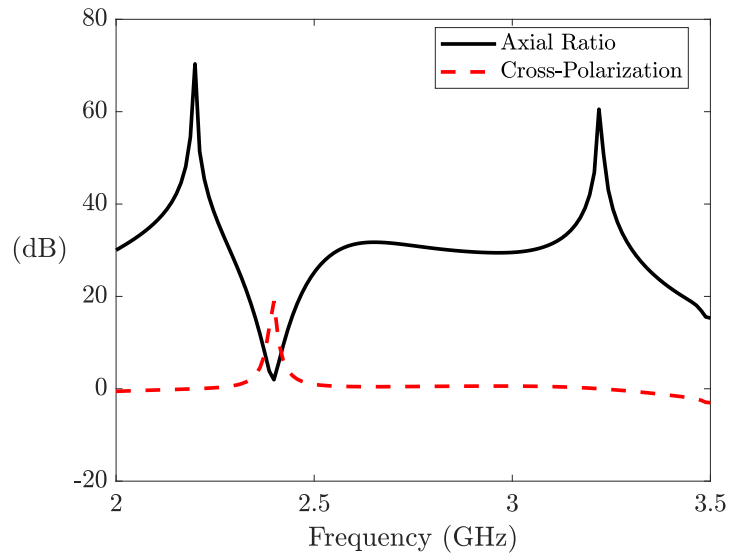
Fig. 5.4: Simulated LHCP-array axial ratio and cross-polarization.
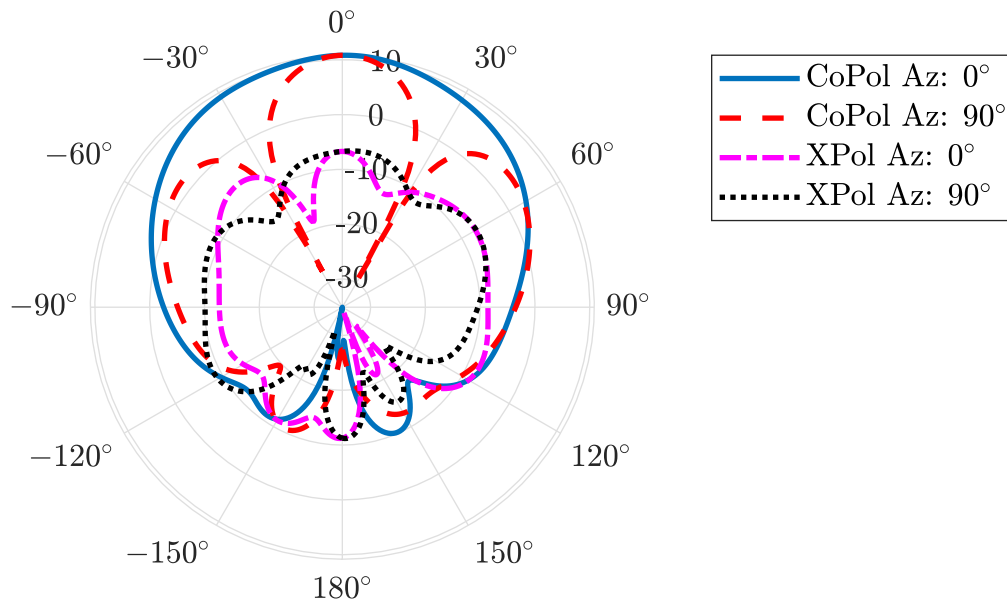
Fig. 5.5: Elevation pattern of 2x2 LHCP array.

In addition to the axial ratio, Figure 5.4 also shows the cross-polarization of the LHCP antenna array. The cross-polarization of the array is near 20 dB, which is lower than the single element (see Figure 4.4), but is still acceptable. Figure 5.5 shows the radiation levels

of CoPol and XPol vs elevation angle through two cuts in Az angle. Near bore-sight, the difference in polarization levels is above 18 dB, which is congruent with Figure 5.4.

5.2.2 Simulated Array Isolation

The look-up and look-down models represented in Figure 5.2 are used to simulate the isolation between the antennas arrays. The S_{21} simulation results are shown in Figure 5.6.
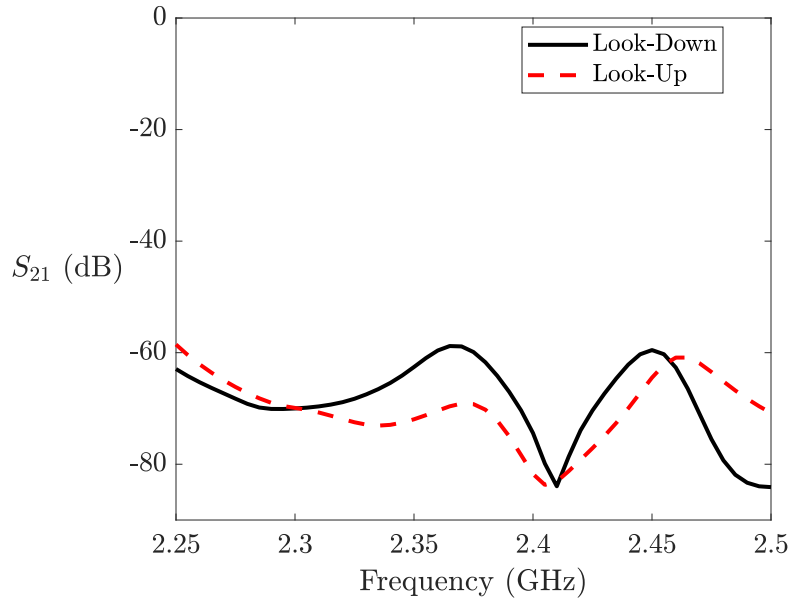
Fig. 5.6: Simulated S_{21} of antenna arrays in look-up and look-down configurations.

At 2.4 GHz, there is 74 dB of isolation when looking down and 81 dB when looking up. These results give confidence that the isolation required by (4.9) can be realized with array configurations, even though the coupling between antenna arrays is more complicated than single-element arrays. The additional suppression achieved using antenna arrays demonstrates that the CW radar can be suppress self-interference below the noise floor even when the SIS realized in the digital and analog domains are lower than the values assumed in the derivation of (4.9).

CHAPTER 6

DESIGN METHODS AND RESULTS: RADAR FRONT-END

Objective 3 of this thesis realizes a functional radar front-end that operates at 2.4 GHz with the antennas or antenna arrays designed in Chapters 4 and 5. To meet Objective 3, this chapter first models the CubeSat-borne, CW radar's capabilities in a power budget. Next, this chapter presents tests to ensure the realized radar meets capabilities specified by the power budget. Lastly, front-end circuitry is designed and built to support the antennas fabricated in Chapter 4 and tested to verify performance.

Time constraints make it impossible to launch and test the radar in space, so ground testing replaces space testing. Ground testing is adequate to show valid results by exploiting ratios in (2.1).

6.1 Power Budget

A power budget provides an analytical representation of a radar's capabilities. The power budget derives from (2.1). To develop the power budget, a mono-static approximation is incorporated. This approximation results in the simplified radar equation

$$SNR = \frac{P_r}{N} = \frac{P_{\text{avg}} G^2 \lambda^2 \sigma}{(4\pi)^3 R^4 k_B T_s B_n}.$$ (6.1)

The CW radar is strictly bi-static because the TX and RX do not share the same antenna. However, some approximations make the radar quasi-mono-static and allow for the model to be described by the mono-static radar equation. These approximations are

- The antennas are designed with the same gain

$$G_t = G_r = G$$ (6.2)

- The distance between antennas, R_d, is much smaller than the range to target R (see Figure 6.1), so

$$R_t = R_r \approx R \tag{6.3}$$

TX G_t P_{avg}

R_t

R

R_d

σ

R_r

RX G_r P_r
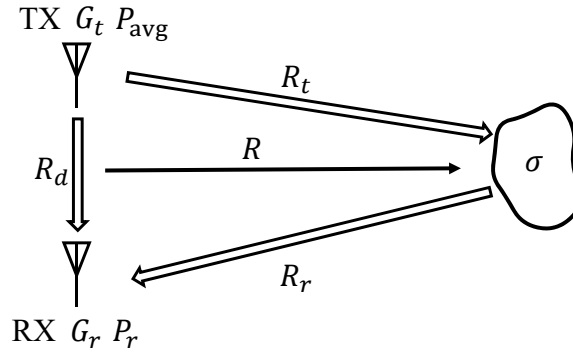
Fig. 6.1: Visualization of parameters specified in radar equation.

It is often convenient to work with (6.1) in decibels

$$
\begin{aligned}
SNR \text{ (dB)} &= P_r - N \text{ (dB)} \\
&= P_{\text{avg}} + 2G + \sigma + 10 \log_{10} \left(\frac{\lambda^2}{4^3 \pi^3 R^4} \right) - N - L \text{ (dB)} \\
&= P_{\text{avg}} + 2G + \sigma + L_s - N - L \text{ (dB)}, \tag{6.4}
\end{aligned}
$$

where:

$L_s = $ Path Loss [dB]

$L = $ Additional Loss [dB].

The additional loss, L, makes up for any inaccuracies due to approximations.

6.1.1 Detectable Targets

Rearranging (6.4) to calculate the minimum detectable RCS of a target when a minimum required SNR, $SNR_{\min}$, is known, results in

$$\sigma = SNR_{\min} - (P_{\text{avg}} + 2G + L_s - N - L) \text{ (dB)}. \qquad (6.5)$$

$SNR_{\min}$ is determined by the detection and false-alarm probabilities specified for the radar (see Appendix B). A radar that implements a coded channel [72] can reduce the required $SNR_{\min}$. P_{avg} is set by Section 3.3, G for the fabricated antennas is calculated in Section 4.3.1, N is derived in Section 4.1.1, and L is arbitrary. Table 6.1 summarizes these parameters for an uncoded channel and Table 6.2 provided these parameters for a coded channel.

Table 6.1: Set parameters for calculating the minimum detectable RCS of an uncoded channel.

Parameter	Value	Units
$SNR_{\min}$	14	dB
P_{avg}	1, 30	W, dBm
G	6.5	dB
N	-93	dBm
L	2	dB

Table 6.2: Set parameters for calculating the minimum detectable RCS of a coded channel.

Parameter	Value	Units
$SNR_{\min}$	5	dB
P_{avg}	1, 30	W, dBm
G	6.5	dB
N	-93	dBm
L	2	dB

Using the parameters from Table 6.1 and a 2.4 GHz radar, Table 6.3 provides the minimum detectable RCS at various ranges and a target that has an equivalent or greater RCS. Likewise, Table 6.4 provides the minimum detectable RCS when using the coded channel described by Table 6.2.

Table 6.3: RCS of detectable objects at various ranges for an uncoded radar channel.

Range (km)	$\sigma(\text{m}^2)$	Detectable Object
0.1	15	0.14 m^2 debris
1	150×10^3	Hubble Space Telescope
4.5	61×10^6	James Webb Space Telescope
10	3×10^9	International Space Station

Table 6.4: RCS of detectable objects at various ranges for a coded radar channel.

Range (km)	$\sigma(\text{m}^2)$	Detectable Object
0.1	1.86	0.05 m^2 debris
1.6	150×10^3	Hubble Space Telescope
7.6	61×10^6	James Webb Space Telescope
20	3×10^9	International Space Station

The equivalent objects in Table 6.3 assume a flat plate target and are found by solving for s in

$$\sigma = \frac{4\pi s^2}{\lambda^2}, \tag{6.6}$$

from Lacomme [73], where:

s = Area of flat-plate target

6.2 Ground Testing: The Uncoded Channel

This section provides the results of tests that verify the detection capabilities outlined by Section 6.1. Due to time and cost constraints, ground tests replace space tests. An anechoic chamber houses the ground tests. The anechoic chamber limits the range of these ground tests to $R = 2.5$ m. For the quasi-mono-static radar equation (6.1) to be applied in the ground tests, the approximation in (6.3) must be valid. The CubeSat model from Section 4.3.2 provides 0.575 meters between the antennas. Applying the Pythagorean theorem to the triangle with lengths R, $0.5R_d$, and R_t or R_r depicted in Figure 6.1, the approximation in (6.3) holds true within 1%. This tolerance is acceptable for ground testing.

Since the range of these ground tests is limited to the size of the anechoic chamber, other parameters in (6.1) are adjusted to maintain the same ratio. Rearranging (6.1) to have all the fixed parameters on the left-hand side of the equation results in

$$\frac{SNR_{\min}(4\pi)^3}{\lambda^2 G^2} = \frac{P_{\text{avg}}\sigma}{NR^4} = \gamma, \tag{6.7}$$

which is denoted as γ. As long as γ remains unchanged, P_{avg}, σ, N, and R can change. For the model of an uncoded channel, $SNR_{\min}$ is 14 dB.

For the ground tests described in this chapter a Hewlett Packard E4433B Signal Generator sources the TX, and an Agilent Technologies CXA N9000A Signal Analyzer acts as the RX. The CXA N9000A has a noise floor of -73 dBm.

Taking the 0.1 km values from Table 6.3 and letting the subscript 1 denote the modified parameters, maintaining the overall ratio γ results in

$$\begin{aligned}
\gamma &= \gamma_1 \\
&= \frac{P_{\mathrm{avg1}}\sigma_1}{N_1 R_1^4} \\
&= \frac{P_{\mathrm{avg1}}\sigma_1}{N(100)\left(\frac{R}{40}\right)^4} \\
&= \frac{P_{\mathrm{avg1}}\sigma_1}{NR^4}\left(\frac{40^4}{100}\right) \\
&= \frac{P_{\mathrm{avg1}}\sigma_1}{NR^4}(25600),
\end{aligned}$$

noting that 2.5 m is one-fortieth of 0.1 km and -73 dBm is 100 times greater than -93 dBm.

A flat plate with area 36×30.5 in^2 (0.9144×0.7747 m^2) acts as the target in the anechoic chamber. From (6.6), this target has $\sigma_1 = 403.58$ m^2, which is 26.9 times greater than 15 m^2. Applying this modified parameter in γ produces

$$\begin{aligned}
\gamma &= \frac{P_{\mathrm{avg1}}\sigma}{NR^4}(26.9 \times 25600) \\
&= \frac{P_{\mathrm{avg1}}\sigma}{NR^4}(688776).
\end{aligned}$$

The γ ratio shows that a 1.45×10^{-6} W (-28.5 dBm) transmit power provides 14 dB of SNR in the ground test.

Figure 6.2 shows the test set-up to verify this ratio. The 6U CubeSat model from Section 4.3.2 holds the antennas.
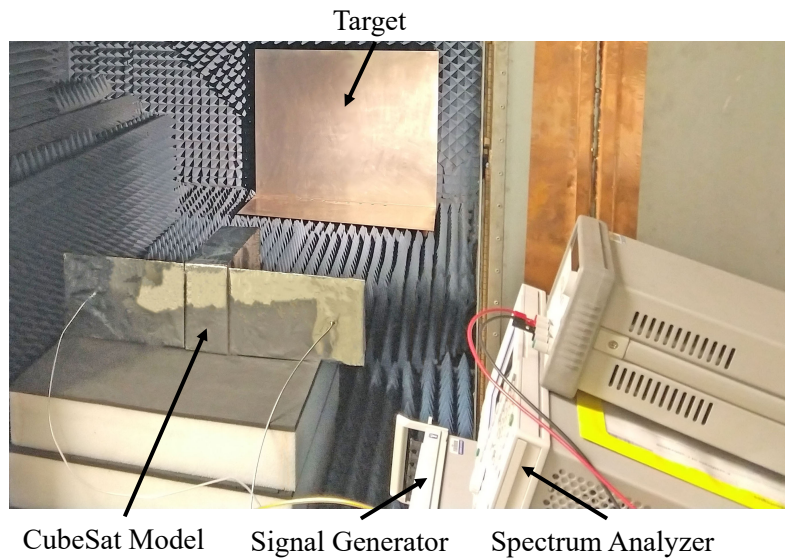
Fig. 6.2: Test set-up to verify the radar's detection capabilities.

An accurate result of the test is identifiable when the detected signal power is -59 dBm (14 dB above the noise).

6.2.1   Initial Test Results

Table 6.5 summarizes the radar parameters for ground testing derived in Section 6.2. Figure 6.3 presents the received power with this set-up and the radar in look-up configuration.

Table 6.5: Parameters for initial ground test.

Parameter	Value	Units
R_1	2.5	m
N_1	-73	dBm
σ_1	403.58	m^2
P_{avg1}	-28.5	dBm

Fig. 6.3: Measured P_r for ground test using parameters from Table 6.5.

The peak of the return power in Figure 6.3 is -64 dBm. This is only 9 dB higher than the noise floor. This does not meet the required received power of -59 dBm to achieve the SNR of 14 dB used in (6.7), and the test fails. Before continuing to test the radar's detection capabilities in the look-down configuration, Section 6.2.2 develops additional tests to verify the radar performance is as presented in Section 6.1.

6.2.2 Target-Effective-Area Test

The results in Section 6.2.1 do not match the expectations derived in Section 6.1. To identify where the tests went wrong, this section analyzes the parameters in (6.7).

Since N_1 and R_1 are fixed by the equipment and testing environment, they are known and cannot be responsible for the error. P_{avg1} is the result of the derivation of γ_1, so P_{avg1} too is not responsible for the error. Thus, σ_1 is the cause of the inaccuracy. The formula (6.6) is accurate, so the conclusion is that the entire plate is not reflecting.

Further tests show when absorbers are placed in front of different regions of the target, some regions decrease the received power while other regions do not. Table 6.6 shows the

additional loss in power when a 4 in. wide absorber is placed over various regions of the target.

Table 6.6: Additional loss due to placing absorber in front of target. Region placement is measured in inches from the left edge of the target.

Placement	0-4 in	4-8 in	8-12 in	12-16 in	16-20 in	20-24 in	24-28 in	28-32 in	32-36 in
Region	1	2	3	4	5	6	7	8	9
Loss	0	0.5	4	10	10	10	4	0.5	0

Table 6.6 shows that the edge regions do not contribute much to the received power. This is due to the geometry of reflection. EM waves that reflect off the target in regions 1, 2, 8, or 9 do not end up near enough to the receive antenna to be detected. Only regions 3-7 reflect waves near enough to the RX antenna to contribute to the received power. This shrinks the effective width of the target to be only 20 in. (0.508 m). The effective RCS, σ_e, from (6.6), is then 127 m^2. Applying σ_e to γ_1 results in

$$
\begin{aligned}
\gamma &= \frac{P_{\text{avg1}}\sigma_e}{NR^4}(25600) \\
&= \frac{P_{\text{avg1}}\sigma}{NR^4}(8.3 \times 25600) \\
&= \frac{P_{\text{avg1}}\sigma}{NR^4}(212585).
\end{aligned}
$$

In this case, a 4.7×10^{-6} W (-23.5 dBm) transmit power preserves the γ ratio in the ground test.

6.2.3 Complete Ground Test

With the error in Section 6.2.1 resolved, the test in Section 6.2.1 is continued to measure P_r for both look-up and look-down configurations. Using the same test set-up as in Figure 6.2, the test now uses the parameters in Table 6.7. Figure 6.3 presents the received power with these parameters.

Table 6.7: Parameters for initial ground test.

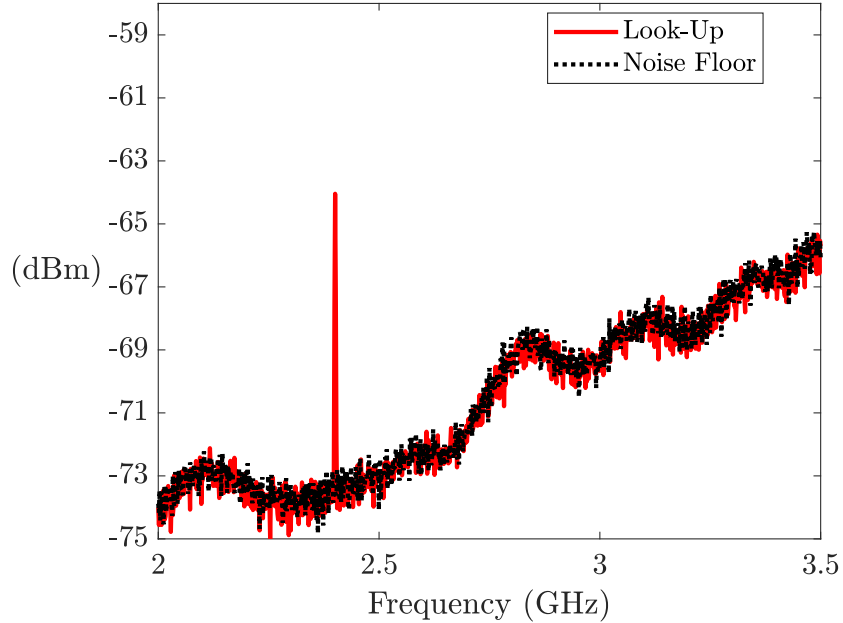| Parameter	Value	Units
R_1	2.5	m
N_1	-73	dBm
σ_e	127	m^2
P_{avg1}	-23.5	dBm
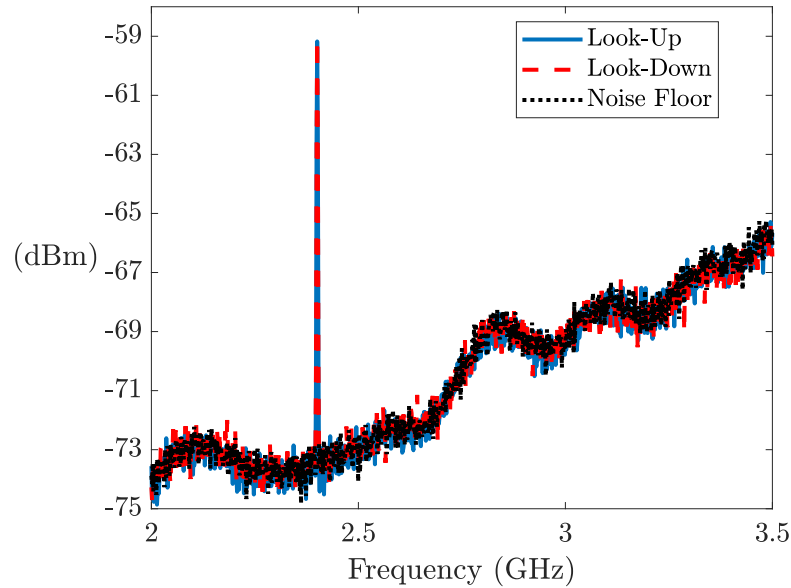
Fig. 6.4: Measured P_r for ground test using parameters from Table 6.7.

The peak of the return power in Figure 6.4 is -59 dBm for both look-up and look-down configurations. Receiving -59 dBm provides more than 14 dB of SNR and verifies that the test successfully models the radar. This result confirms that the prototype radar meets the detection capabilities outlined in Table 6.3 when in look-up and look-down configurations.

6.3 Ground Testing: The Coded Channel

A coded channel can lower the minimum SNR requirement while maintaining the desired probabilities of detection and false-alarm [72]. This allows the radar to detect targets with a smaller RCS. The manipulation of the ratio in (6.7) for a coded channel follows the same steps as shown in Section 6.2.

Taking the 0.1 km values from Table 6.4 with $SNR_{\min} = 5$ dB it can be shown that in the look-up configuration, which has 57 dB of isolation, the radar can detect a flat plate with area 6×6 in^2 (0.1524×0.1524 m^2) and $\sigma = 0.4338$ when $P_{\mathrm{avg}} = -20$ dBm. This transmit power ensures that the self-interference is below the noise floor. The test set-up to verify these calculations is shown in Figure 6.5. Figure 6.6 shows that without a target, no self-interference appears above the noise floor. When a target is present, 6 dB of SNR is achieved which is greater than the required coded $SNR_{\min}$ of 5 dB.

When performing the same test in the look-down configuration there is only 41 dB of isolation, so the self-interference is not pushed below the noise floor. This has the result of raising the noise floor to the level of the self-interference and lowering the achievable SNR. Figure 6.7 shows that the self-interference is 8 dB above the noise floor. When there is also a target to detect, the received power is greater than the self-interference, but only by 3 dB.
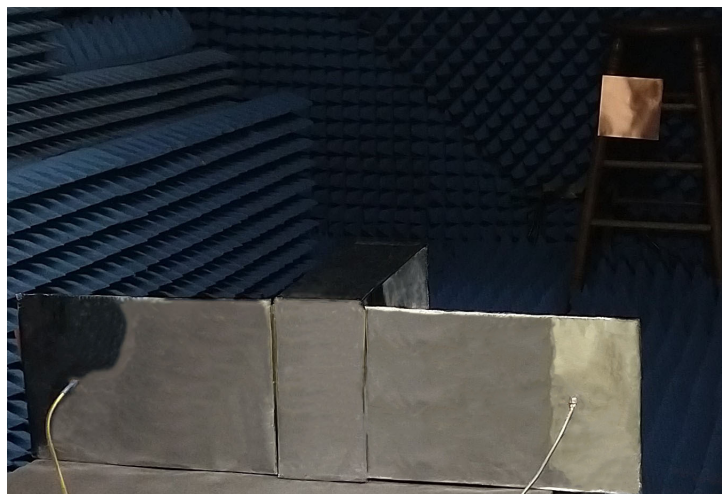
Fig. 6.5: Test set-up to verify detection of a small target.
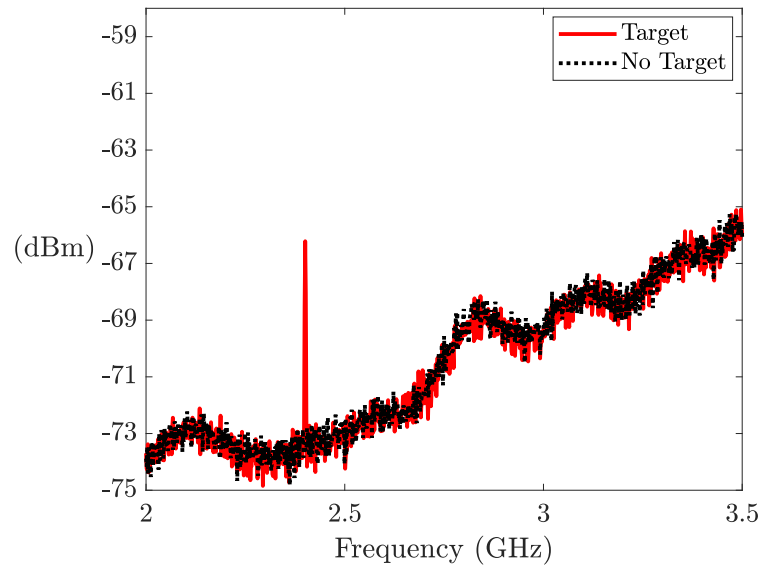
Fig. 6.6: Measured P_r for ground test modeling a coded channel when looking up.
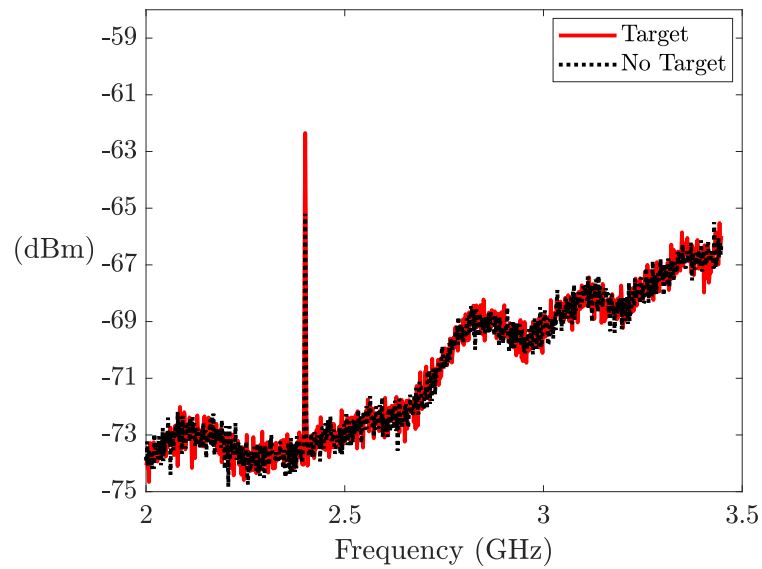
Fig. 6.7: Measured P_r for ground test modeling a coded channel when looking down.

The 3 dB of SNR achieved in Figure 6.7 is less than the minimum 5 dB required by the coded channel model, so the target cannot be detected. This demonstrates the significance of providing enough isolation to suppress the self-interference below the noise floor of the RX.

6.4   Front-End Prototype

This section provides the design, implementation, and results of a radar front-end. A radar front-end consists of the electronics between the digital-to-analog-converter (DAC) and the antenna (ANT) in the TX channel and between the antenna and the ADC in the RX channel. The front-end also includes circuitry for a local oscillator (LO) if required. A typical, front-end design for both TX and RX includes a cascade of amplifiers, filters, and mixers (MIX) (see Figure 6.8). The main amplifier in the TX channel is the high power amplifier (HPA). The LNA is the main amplifier in the RX channel. Between each component shown in Figure 6.8, the proper addition of amplifiers and attenuators keep the power levels entering each component within levels specified by the component's datasheet.

(a) TX front-end.
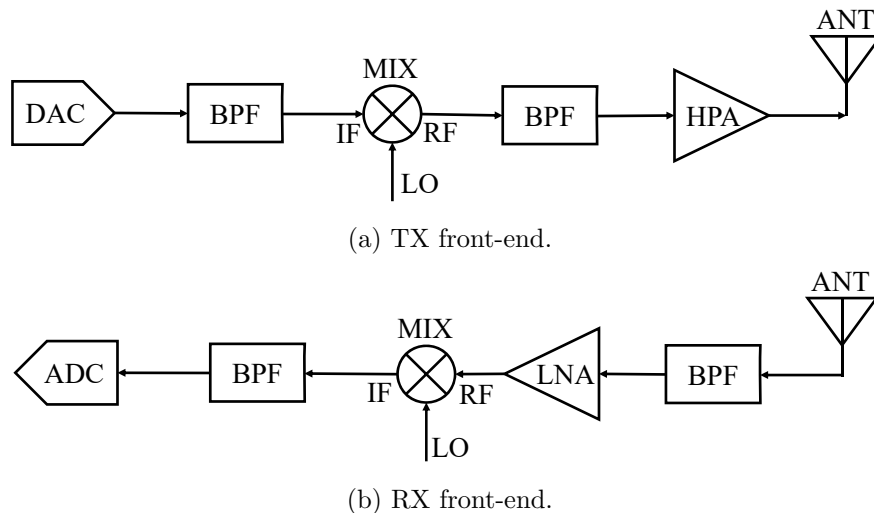
(b) RX front-end.

Fig. 6.8: Front-end designs for the (a) TX and (b) RX channels of a generic radar.

The front-end of the radar design is simplified for ground testing. A Hewlett Packard E4433B Signal Generator replaces the entire TX front-end. The RX front-end and LO circuitry are reduced to the components shown in Figure 6.9.
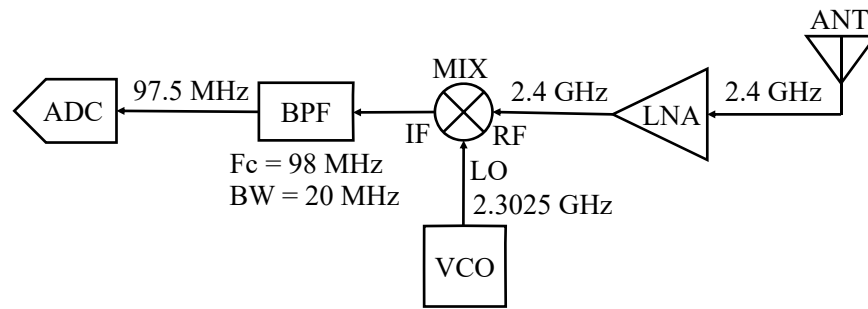
Fig. 6.9: Front-end design of reduced RX channel.

The filter located immediately after the antenna is removed because the anechoic chamber ensures that the only signal picked up by the RX is the one transmitted. The LO is comprised of a single component, a voltage-controlled oscillator (VCO). This design is realized in Figure 6.10 with commercial-off-the-shelf components. The components are characterized in detail in Appendix C.
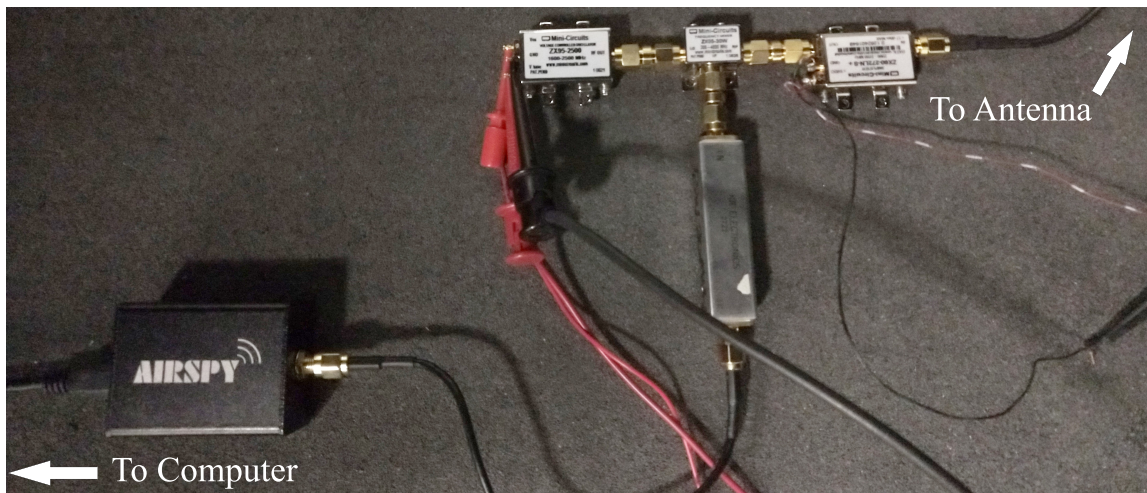
Fig. 6.10: Realization of radar front-end.

The power consumption of the front-end is an important characteristic, especially when the radar is implemented on a CubeSat. Table 6.8 shows the power consumed by each component and the channel as a whole.

Table 6.8: Power consumed by radar front-end.

Component	Supply Voltage (V)	Supply Current (mA)	Power Consumed (W)
LNA	5	60	0.3
VCO	12	25	0.3
ADC	5	340	1.7
Total	-	425	2.3

To verify performance, the Agilent Technologies CXA N9000A Signal Analyzer replaces the ADC. The front-end circuit is then tested to verify the target used in Section 6.2 is detectable in both look-up and look-down antenna configurations (see Sections 4.2.2 and 4.3.2) with an uncoded channel. Figure 6.11 shows the received spectrum measured by a signal analyzer immediately before the ADC.
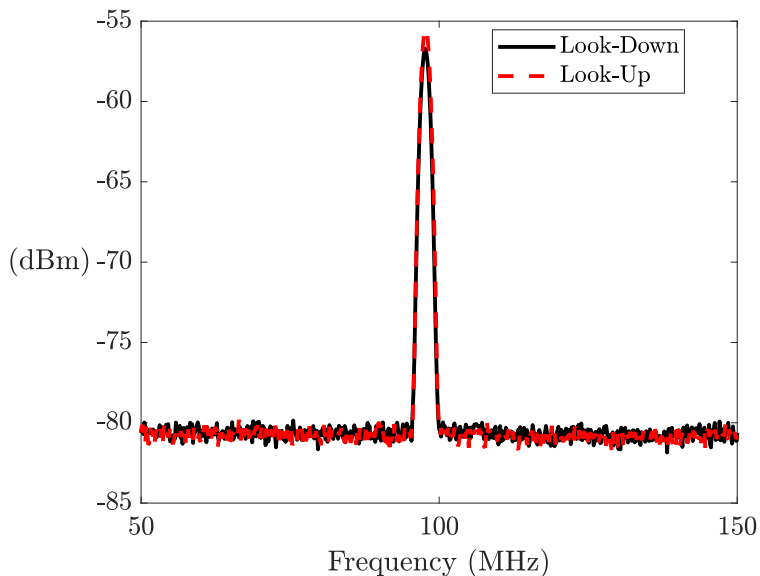
Fig. 6.11: Spectrum of received signal entering the ADC.

The power level of the received signal at the output of the front-end in both configurations is near -56 dBm. The noise floor has decreased due to the reduction in bandwidth of the signal analyzer to only 100 MHz, see (4.1).

6.4.1 Digitization

The final stage of the front-end is digitization with an ADC. Digitization samples the received signals in preparation for a computer or field-programmable gate array to apply signal processing algorithms to the data to find or track targets, form images, or determine weather characteristics depending on the radar's purpose. The various algorithms for these applications are outside the scope of Objective 3, but the digitization is not.

The Airspy R2 is selected as the ADC for its low cost and ease of use. The free SDR# (pronounced SDR Sharp) software is compatible with the Airspy R2. SDR# displays 8 MHz bandwidth of the received signal's power spectrum and spectrogram (see Figure 6.12). Various demodulation types are available. The "RAW" option shows the unmodified signal received by the Airspy.
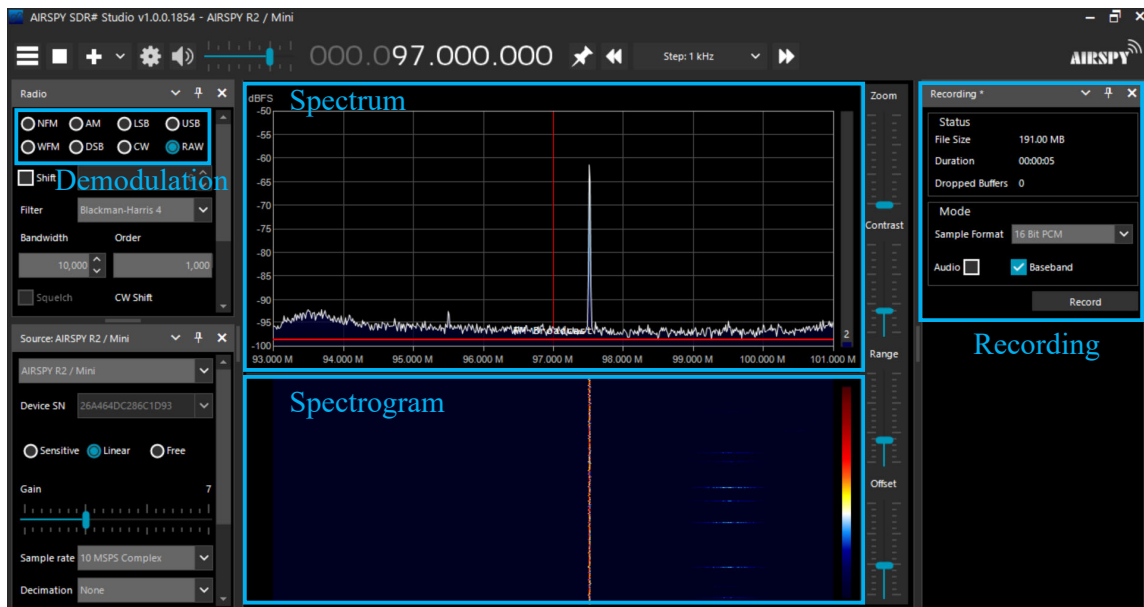
Fig. 6.12: SDR# software display.

SDR# provides recording capabilities that output the sampled, time-domain signal as a .wav file. These recordings are then ready for further processing. Figure 6.13 shows the power spectrum of the signals recorded by SDR#.

Sampling has base-banded the spectrum. The frequency marked with a red line in the

64

spectrum of Figure 6.12 has been mapped to zero hertz, placing the signal of interest at about 0.5 MHz. The power level at the peak of the signal is -59 dBm, which is 3 dB lower than the measurement on the spectrum analyzer. This difference shows that digitization has some loss.
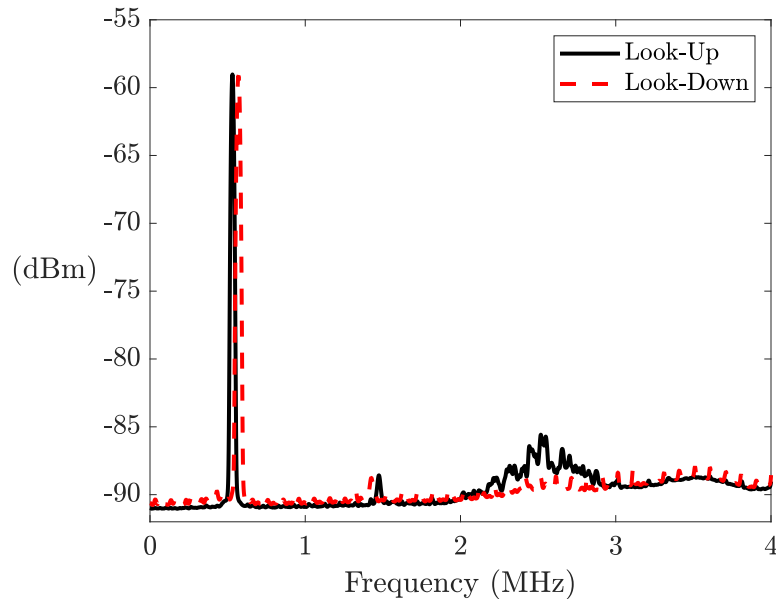
Fig. 6.13: Power spectrum of digitized receive signal.

There is also a noticeable difference in frequency between the two peaks in Figure 6.13. As shown, the difference is about 50 kHz. This is the result of the thermal instability of the Airspy R2. As the temperature changes, the internal circuitry behaves differently. The time it takes to switch the configuration of the antennas is long enough that the increased temperature of the Airspy R2 creates a noticeable shift in frequency. The frequency drift is slow but noticeable. Figure 6.14 shows the measured frequency shift over time. The linear trend line is describe by

$$y = 1.433 \times 10^{-3}x + 97.75. \tag{6.8}$$

The quadratic trend line is described by

$$y = -2.755 \times 10^{-6}x^2 + 2.232 \times 10^{-3}x + 97.72. \tag{6.9}$$
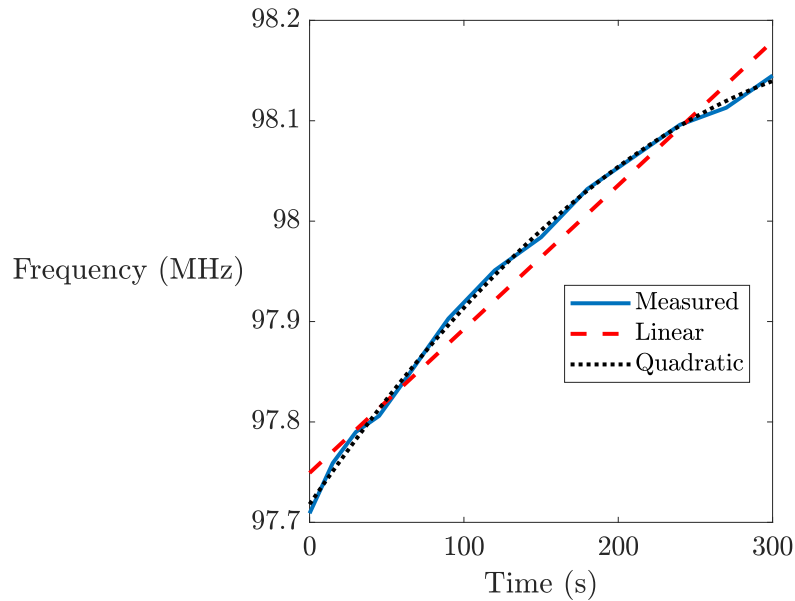
Fig. 6.14: Measured frequency drift of Airspy R2.

(6.8) shows that over the duration of the measurements the frequency drifted 1.4 kHz/s. However, the quadratic trend line fits the measurements better. This suggests that the frequency drift slows down over time. (6.9) predicts that the frequency drift should eventually stop after 405 s.

The thermal sensitivity depicted in Figure 6.14 is not exclusive to the Airspy R2. A consciousness of the system temperature and a way to maintain the temperature at a desired level are important to developing a radar system but are outside the scope of Objective 3.

The front-end developed in this chapter is not immediately implementable on a Cube-Sat. Special components designed to withstand the harsh environment of space are required, but the layout of the front-end is comparable to one that can go into space. With space-verified components, a front-end like this one could operate in space. Additionally, less power-hungry components should take the place of the Airspy R2 in a CubeSat-borne radar.

CHAPTER 7

CONCLUSION

The NASA JPL's RainCube was the first, and is currently the only, CubeSat-borne radar. This thesis presents a radar design that improves the characteristics of CubeSat-borne radars. The RainCube was limited by dedicating 25% of its volume to the stowed antenna, which became wasted space after deployment. The RainCube also utilized pulse-Doppler waveform radar that requires high peak-power pulses. This thesis presents a radar design that overcomes the limitations of a deployable antenna and high peak power.

The radar design in this work uses two antennas that are integrated on the satellite's solar panels. This removes the need for antenna storage and deployment. The radar also decreases the required transmit power and increases the CubeSat's battery life by transmitting and receiving simultaneously and continuously. To overcome the self-interference that continuous-waveform radar faces, a novel self-interference suppression technique is successfully implemented by combining physical-separation and polarization-diversity isolation methods.

The amount of suppression required is calculated to be at least 39 dB. Test show that the combination of physical separation and circular-polarization diversity achieves up to 65 dB of isolation in simulation and 57 dB with fabricated antennas. This verifies that the combination of physical-separation and polarization-diversity isolation methods provide enough isolation for a continuous-waveform radar to be realized on a CubeSat.

Antenna arrays are common in radar systems because they increase the directivity of the radar. This provides more gain in the direction of interest and less clutter in the received signal. Understanding the isolation achievable when using antenna arrays instead of single-element antennas is of interest. The concern is that the elements of an antenna array at the receiver are not the same distance from the elements of a transmit-antenna array.

Simulation shows that even more isolation is achievable with the antenna array than with the single element antennas. The isolation is above 81 dB. These simulations assure that combining physical-separation and polarization-diversity isolation methods to antenna arrays is feasible and improves performance.

To verify the radar's capabilities to detect targets in space, ground tests are performed. These ground tests use a different target range, system noise floor, radar cross-section of the target, and transmit power than intended for space applications. By maintaining the overall ratio of these parameters described by (6.7), the ground tests measuring the radar's capabilities are valid for space applications.

A functional radar front-end is built for the receive channel. This front-end produces a digitized signal ready for signal processing. Tests show that the front-end operates as designed. The front-end is compact and, except for the Airspy R2, does not consume a lot of power. A similar front-end, with space-grade components, could support a continuous-waveform radar on a CubeSat.

This work presents a good first step to improving the capabilities of CubeSat-borne radar. Future efforts can further develop this research by raising the operating frequency, implementing antenna arrays, and developing a full radar front-end.

The antennas presented are designed to operate at 2.4 GHz. This makes fabrication feasible with the resources accessible to the research. Future efforts can design antennas to operate at higher frequencies, miniaturizing the design and making implementation on a CubeSat more feasible.

With a radar system operating at a higher frequency, the next step is to design antenna arrays that fit within the size constraints of the solar panels. These arrays can then be fabricated and tested to verify the simulated results of Chapter 5.

The radar front-end design can be improved to include a full transmitter instead of using a signal generator. It would also be interesting to design a power distribution system that fits on the CubeSat. With a full receiver, transmitter, and power supply, future works can verify that the space and power these electronics require are sustainable on a CubeSat.

The development of a CubeSat-borne, continuous-waveform radar opens the door to future innovations involving radar on small platforms. Platforms like small aircraft, drones, and hand-held devices benefit from the improved power usage, battery life, small form factor, and isolation of the antenna designs presented in this thesis and suggested for future research.

REFERENCES

[1] P. Lacomme, J.-P. Hardange, J.-C. Marchais, and E. Normant, "15 - SYNTHETIC APERTURE RADAR," in *Air and Spaceborne Radar Systems*, P. Lacomme, J.-P. Hardange, J.-C. Marchais, and E. Normant, Eds. Norwich, NY: William Andrew Publishing, Jan. 2001, pp. 233–264, https://doi.org/10.1016/B978-189112113-5.50017-6.

[2] NASA Jet Propulsion Laboratory, "RainCube: Radar in a CubeSat," https://www.jpl.nasa.gov/cubesat/missions/raincube.php.

[3] E. Peral, S. Tanelli, S. Statham, S. Joshi, T. Imken, D. Price, J. Sauder, N. Chahat, and A. Williams, "RainCube: The first ever radar measurements from a CubeSat in space," *Journal of Applied Remote Sensing*, vol. 13, no. 3, p. 032504, Jun. 2019, https://doi.org/10.1117/1.JRS.13.032504.

[4] Y. Rahmat-Samii, V. Manohar, J. M. Kovitz, R. E. Hodges, G. Freebury, and E. Peral, "Development of Highly Constrained 1 m *Ka* -Band Mesh Deployable Offset Reflector Antenna for Next Generation CubeSat Radars," *IEEE Transactions on Antennas and Propagation*, vol. 67, no. 10, pp. 6254–6266, Oct. 2019, https://doi.org/10.1109/TAP.2019.2920223.

[5] V. Knap, L. K. Vestergaard, and D.-I. Stroe, "A Review of Battery Technology in CubeSats and Small Satellite Solutions," *Energies*, vol. 13, no. 16, p. 4097, Jan. 2020, https://doi.org/10.3390/en13164097.

[6] J.-W. Lee, Y. K. Anguchamy, and B. N. Popov, "Simulation of charge–discharge cycling of lithium-ion batteries under low-earth-orbit conditions," *Journal of Power Sources*, vol. 162, no. 2, pp. 1395–1400, Nov. 2006, https://doi.org/10.1016/j.jpowsour.2006.07.045.

[7] S. Farahani, "Chapter 6 - Battery Life Analysis," in *ZigBee Wireless Networks and Transceivers*, S. Farahani, Ed. Burlington: Newnes, Jan. 2008, pp. 207–224, https://doi.org/10.1016/B978-0-7506-8393-7.00006-6.

[8] L. Blain, "How to extend the life of your lithium-ion batteries," https://newatlas.com/electronics/extend-life-lithium-ion-batteries/, Feb. 2020.

[9] F. Hoffart, "Proper Care Extends Li-Ion Battery Life," https://www.powerelectronics.com/markets/mobile/article/21859861/proper-care-extends-liion-battery-life,   Apr. 2008.

[10] T. Yekan and R. Baktur, "Conformal Integrated Solar Panel Antennas: Two effective integration methods of antennas with solar cells." *IEEE Antennas and Propagation Magazine*, vol. 59, no. 2, pp. 69–78, Apr. 2017, https://doi.org/10.1109/MAP.2017.2655577.

[11] N. Levanon, "Radar," in *Encyclopedia of Physical Science and Technology*, 3rd ed., R. A. Meyers, Ed. New York: Academic Press, 2003, vol. 13, pp. 497–510, https://doi.org/10.1016/B0-12-227410-5/00973-X.

[12] M. Parker, "Chapter 18: Radar Basics," in *Digital Signal Processing 101*, 2nd ed. Newnes, Jun. 2017, https://learning.oreilly.com/library/view/digital-signal-processing/9780128114544/XHTML/B9780128114537000184/B9780128114537000184.xhtml.

[13] C. A. Balanis, "Chapter 2: Fundamental Parameters and Figures-of-Merit of Antennas," in *Antenna Theory: Analysis and Design*, 4th ed. Hoboken, NJ: John Wiley & Sons, Incorporated, 2016, pp. 25–126, http://ebookcentral.proquest.com/lib/usu/detail.action?docID=4205879.

[14] I. G. Cumming and F. H.-c. Wong, "Chapter 1: Introduction," in *Digital Processing of Synthetic Aperture Radar Data: Algorithms and Implementation*, 1st ed. Artech House, Jan. 2005, pp. 3–20.

[15] B. R. Mahafza, *Radar Systems Analysis and Design Using Matlab*. Boca Raton: Chapman & Hall/CRC, 2000.

[16] O. N. Alrabadi, A. D. Tatomirescu, M. B. Knudsen, M. Pelosi, and G. F. Pedersen, "Breaking the Transmitter–Receiver Isolation Barrier in Mobile Handsets With Spatial Duplexing," *IEEE Transactions on Antennas and Propagation*, vol. 61, no. 4, pp. 2241–2251, Apr. 2013, https://doi.org/10.1109/TAP.2012.2232897.

[17] P. Lacomme, J.-P. Hardange, J.-C. Marchais, and E. Normant, "1 - THE HISTORY AND BASIC PRINCIPLES OF RADAR," in *Air and Spaceborne Radar Systems*, P. Lacomme, J.-P. Hardange, J.-C. Marchais, and E. Normant, Eds. Norwich, NY: William Andrew Publishing, Jan. 2001, pp. 1–12, https://doi.org/10.1016/B978-189112113-5.50003-6.

[18] M. Parker, "Chapter 19: Pulse Doppler Radar," in *Digital Signal Processing 101*, 2nd ed. Newnes, Jun. 2017, https://learning.oreilly.com/library/view/digital-signal-processing/9780128114544/XHTML/B9780128114537000184/B9780128114537000184.xhtml.

[19] C. Wolff, "UWB-Radar," https://www.radartutorial.eu/02.basics/UWB%20Radar.en.html.

[20] R. Lian, T.-Y. Shih, Y. Yin, and N. Behdad, "A High-Isolation, Ultra-Wideband Simultaneous Transmit and Receive Antenna With Monopole-Like Radiation Characteristics," *IEEE Transactions on Antennas and Propagation*, vol. 66, no. 2, pp. 1002–1007, Feb. 2018, https://doi.org/10.1109/TAP.2017.2784447.

[21] J. C. Wise, "A Perspective on EW Receiver Design," Air Power Australia, Tech. Rep. APA-TR-2009-1102, Nov. 2009, http://www.ausairpower.net/APA-Maritime-ESM.html.

[22] A. D. Naval Air Warfare Center Weapons Division, "Electronic Warfare and Radar Systems Engineering handbook," http://ed-thelen.org/pics/Radar-NAWCWD-TP-8347.pdf, Oct. 2013.

[23] H.-R. Chen, "FMCW Radar Jamming Techniques and Analysis," Ph.D. dissertation, NAVAL POSTGRADUATE SCHOOL, Monteryt, CA, USA, Sep. 2013, https://apps.dtic.mil/sti/citations/ADA589567.

[24] S. Pisa, E. Pittella, and E. Piuzzi, "A survey of radar systems for medical applications," *IEEE Aerospace and Electronic Systems Magazine*, vol. 31, no. 11, pp. 64–81, Nov. 2016, https://doi.org/10.1109/MAES.2016.140167.

[25] A. S. D. Lopes, "Bio-Radar Applications for Remote Vital Signs Monitoring," Ph.D. dissertation, NOVA University of Lisbon, Feb. 2021, https://run.unl.pt/handle/10362/118695.

[26] M. Inggs, H. Griffiths, F. Fioranelli, M. Ritchie, and K. Woodbridge, "Multistatic radar: System requirements and experimental validation," in *2014 International Radar Conference*, Oct. 2014, pp. 1–6, https://doi.org/10.1109/RADAR.2014.7060435.

[27] M. A. Richards, "9. Introduction to Beamforming and Space-Time Adaptive Processing," in *Fundamentals of Radar Signal Processing*. McGraw-Hill Professional, Jun. 2005, https://mhebooklibrary.com/doi/book/10.1036/0071444742.

[28] C. Baker and H. Griffiths, "BISTATIC AND MULTISTATIC RADAR SENSORS FOR HOMELAND SECURITY," in *Advances in Sensing with Security Applications*, J. Byrnes and G. Ostheimer, Eds. Dordrecht: Kluwer Academic Publishers, 2006, vol. 2, pp. 1–22, http://link.springer.com/10.1007/1-4020-4295-7_01.

[29] A. Sabharwal, P. Schniter, D. Guo, D. W. Bliss, S. Rangarajan, and R. Wichman, "In-Band Full-Duplex Wireless: Challenges and Opportunities," *IEEE Journal on Selected Areas in Communications*, vol. 32, no. 9, pp. 1637–1652, Sep. 2014, https://doi.org/10.1109/JSAC.2014.2330193.

[30] P. Lacomme, J.-P. Hardange, J.-C. Marchais, and E. Normant, "8 - AIR-TO-AIR DETECTION," in *Air and Spaceborne Radar Systems*, P. Lacomme, J.-P. Hardange, J.-C. Marchais, and E. Normant, Eds. Norwich, NY: William Andrew Publishing, Jan. 2001, pp. 115–157, https://doi.org/10.1016/B978-189112113-5.50010-3.

[31] C. Wolff, "Continuous Wave Radar," https://www.radartutorial.eu/02.basics/Continuous%20Wave%20Radar.en.html.

[32] I. G. Cumming and F. H.-c. Wong, "Chapter 3: Pulse Compression of Linear FM Signals," in *Digital Processing of Synthetic Aperture Radar Data: Algorithms and Implementation*, 1st ed. Artech House, Jan. 2005, pp. 3–20.

[33] M. Parker, "Chapter 20: Automotive Radar," in *Digital Signal Processing 101*, 2nd ed. Newnes, Jun. 2017, https://learning.oreilly.com/library/view/digital-signal-processing/9780128114544/XHTML/B9780128114537000184/B9780128114537000184.xhtml.

[34] J. I. Choi, M. Jain, K. Srinivasan, P. Levis, and S. Katti, "Achieving single channel, full duplex wireless communication," in *Proceedings of the Sixteenth Annual International Conference on Mobile Computing and Networking*, ser. MobiCom '10. New York, NY, USA: Association for Computing Machinery, Sep. 2010, pp. 1–12, https://doi.org/10.1145/1859995.1859997.

[35] H. Nawaz and I. Tekin, "Dual-Polarized, Differential Fed Microstrip Patch Antennas With Very High Interport Isolation for Full-Duplex Communication," *IEEE Transactions on Antennas and Propagation*, vol. 65, no. 12, pp. 7355–7360, Dec. 2017, https://doi.org/10.1109/TAP.2017.2765829.

[36] D. Bharadia and S. Katti, "Full Duplex {MIMO} Radios," in *11th {USENIX} Symposium on Networked Systems Design and Implementation ({NSDI} 14)*, Seattle, WA, USA, Apr. 2014, pp. 359–372, https://www.usenix.org/conference/nsdi14/technical-sessions/bharadia.

[37] D. Wu, Y. Zang, H. Luyen, M. Li, and N. Behdad, "A Compact, Low-Profile Simultaneous Transmit and Receive Antenna With Monopole-Like Radiation Characteristics," *IEEE Antennas and Wireless Propagation Letters*, vol. 18, no. 4, pp. 611–615, Apr. 2019, https://doi.org/10.1109/LAWP.2019.2898220.

[38] A. T. Wegener, "Broadband near-field filters for Simultaneous Transmit and Receive in a small two-dimensional array," in *2014 IEEE MTT-S International Microwave Symposium (IMS2014)*, Jun. 2014, pp. 1–3, https://doi.org/10.1109/MWSYM.2014.6848672.

[39] A. T. Wegener and W. J. Chappell, "Simultaneous Transmit And Receive with a small planar array," in *2012 IEEE/MTT-S International Microwave Symposium Digest*, Jun. 2012, pp. 1–3, https://doi.org/10.1109/MWSYM.2012.6259663.

[40] M. A. Elmansouri, A. J. Kee, and D. S. Filipovic, "Wideband Antenna Array for Simultaneous Transmit and Receive (STAR) Applications," *IEEE Antennas and Wireless Propagation Letters*, vol. 16, pp. 1277–1280, 2017, https://doi.org/10.1109/LAWP.2016.2632737.

[41] E. A. Etellisi, M. A. Elmansouri, and D. S. Filipović, "Wideband Multimode Monostatic Spiral Antenna STAR Subsystem," *IEEE Transactions on Antennas and Propagation*, vol. 65, no. 4, pp. 1845–1854, Apr. 2017, https://doi.org/10.1109/TAP.2017.2670362.

[42] E. Yetisir, C.-C. Chen, and J. L. Volakis, "Wideband Low Profile Multiport Antenna With Omnidirectional Pattern and High Isolation," *IEEE Transactions on Antennas and Propagation*, vol. 64, no. 9, pp. 3777–3786, Sep. 2016, https://doi.org/10.1109/TAP.2016.2583468.

[43] A. Raghavan, E. Gebara, E. Tentzeris, and J. Laskar, "Analysis and design of an interference canceller for collocated radios," *IEEE Transactions on Microwave Theory and Techniques*, vol. 53, no. 11, pp. 3498–3508, Nov. 2005, https://doi.org/10.1109/TMTT.2005.859042.

[44] A. Raghavan, S. Chandramouli, E. Gebara, and J. Laskar, "A low additive noise interference canceller for high sensitivity applications," in *2008 IEEE Radio and Wireless Symposium*, Jan. 2008, pp. 45–48, https://doi.org/10.1109/RWS.2008.4463424.

[45] D. A. Weston, "Antenna-to-Antenna Coupling On An Aircraft: Mitigation Techniques," EMC Consulting, Inc., Merrickville, Ontario, Canada, Tech. Rep., 2012, https://interferencetechnology.com/antenna-to-antenna-coupling-on-an-aircraft-mitigation-techniques/.

[46] S. Ahmed and M. Faulkner, "Optimized Interference Canceling for Colocated Base Station Transceivers," *IEEE Transactions on Vehicular Technology*, vol. 60, no. 9, pp. 4175–4183, Nov. 2011, https://doi.org/10.1109/TVT.2011.2171010.

[47] R. Lian, Z. Wang, Y. Yin, J. Wu, and X. Song, "Design of a Low-Profile Dual-Polarized Stepped Slot Antenna Array for Base Station," *IEEE Antennas and Wireless Propagation Letters*, vol. 15, pp. 362–365, 2016, https://doi.org/10.1109/LAWP.2015.2446193.

[48] Y. Li, Z. Zhang, W. Chen, Z. Feng, and M. F. Iskander, "A Dual-Polarization Slot Antenna Using a Compact CPW Feeding Structure," *IEEE Antennas and Wireless Propagation Letters*, vol. 9, pp. 191–194, 2010, https://doi.org/10.1109/LAWP.2010.2044865.

[49] J. Sarrazin, Y. Mahe, S. Avrillon, and S. Toutain, "Collocated Microstrip Antennas for MIMO Systems With a Low Mutual Coupling Using Mode Confinement," *IEEE Transactions on Antennas and Propagation*, vol. 58, no. 2, pp. 589–592, Feb. 2010, https://doi.org/10.1109/TAP.2009.2037690.

[50] J.-M. Kim and J.-G. Yook, "A parallel-plate-mode suppressed meander slot antenna with plated-through-holes," *IEEE Antennas and Wireless Propagation Letters*, vol. 4, pp. 118–120, 2005, https://doi.org/10.1109/LAWP.2005.846421.

[51] J. Sarrazin, Y. Mahe, S. Avrillon, and S. Toutain, "Four co-located antennas for MIMO systems with a low mutual coupling using mode confinement," in *2008 IEEE Antennas and Propagation Society International Symposium*, Jul. 2008, pp. 1–4, https://doi.org/10.1109/APS.2008.4619401.

[52] D. Wu, S. W. Cheung, Q. L. Li, and T. I. Yuk, "Decoupling using diamond-shaped patterned ground resonator for small MIMO antennas," *IET Microwaves, Antennas & Propagation*, vol. 11, no. 2, pp. 177–183, 2017, https://doi.org/10.1049/iet-map.2016.0400.

[53] J. B. O. de Araújo, V. P. R. M. Souza, T. N. Ferreira, L. J. de Matos, G. L. Siqueira, J. M. Souza, and M. W. B. da Silva, "Mutual Coupling Reduction in Phased Array Antennas Applying High-Impedance Surface at X Band," *Journal of Microwaves, Optoelectronics and Electromagnetic Applications*, vol. 19, pp. 118–128, Mar. 2020, https://doi.org/10.1590/2179-10742020v19i11773.

[54] M.-C. Tang, S. Xiao, B. Wang, J. Guan, and T. Deng, "Improved Performance of a Microstrip Phased Array Using Broadband and Ultra-Low-Loss Metamaterial Slabs,"

IEEE Antennas and Propagation Magazine, vol. 53, no. 6, pp. 31–41, Dec. 2011, https://doi.org/10.1109/MAP.2011.6157712.

[55] S. Zhu, H. Liu, and P. Wen, "A New Method for Achieving Miniaturization and Gain Enhancement of Vivaldi Antenna Array Based on Anisotropic Metasurface," *IEEE Transactions on Antennas and Propagation*, vol. 67, no. 3, pp. 1952–1956, Mar. 2019, https://doi.org/10.1109/TAP.2019.2891220.

[56] D. Esser, B. Solan, and H. Chaloupka, "Improved antenna isolation in transmit/receive applications," in *German Microwave Conference GeMIC2006*, Jan. 2006, p. 5, https://www.semanticscholar.org/paper/Improved-Antenna-Isolation-in-Transmit-%2F-Receive-Esser-Solan/d8b1e37dc437b2f3bf9232e82799caf7966969fa#related-papers.

[57] E. Janssen, D. Milosevic, M. Herben, and P. Baltus, "Increasing Isolation Between Colocated Antennas Using a Spatial Notch," *IEEE Antennas and Wireless Propagation Letters*, vol. 10, pp. 552–555, 2011, https://doi.org/10.1109/LAWP.2011.2158510.

[58] K. Kolodziej, P. Hurst, A. Fenn, and L. Parad, "Ring array antenna with optimized beamformer for Simultaneous Transmit And Receive," in *Proceedings of the 2012 IEEE International Symposium on Antennas and Propagation*, Jul. 2012, pp. 1–2, https://doi.org/10.1109/APS.2012.6349146.

[59] E. A. Etellisi, M. A. Elmansouri, and D. S. Filipovic, "Wideband Monostatic Simultaneous Transmit and Receive (STAR) Antenna," *IEEE Transactions on Antennas and Propagation*, vol. 64, no. 1, pp. 6–15, Jan. 2016, https://doi.org/10.1109/TAP.2015.2497356.

[60] T. Johnsen and K. E. Olsen, "Bi- and Multistatic Radar," NORWEGIAN DEFENCE RESEARCH ESTABLISHMENT KJELLER, Tech. Rep., Sep. 2006, https://apps.dtic.mil/sti/citations/ADA470685.

[61] S. Isaacson, "Enhancement of radar signals by double bounce circular polarization," in *1958 IRE International Convention Record*, vol. 9, Mar. 1961, pp. 10–16.

[62] P. Z. Peebles, Jr., "Radar rain clutter cancellation bounds using circular polarization," in *International Radar Conference*, Jan. 1975, pp. 210–214, https://ui.adsabs.harvard.edu/abs/1975inra.conf..210P.

[63] A. B. Schneider and P. D. L. Williams, "Circular polarization in radars - An assessment of rain clutter reduction and likely loss of target performance," *Radio and Electronic Engineer*, vol. 47, pp. 11–29, Feb. 1977, https://ui.adsabs.harvard.edu/abs/1977RaEE..47...11S.

[64] E. Torlaschi and A. R. Holt, "A comparison of different polarization schemes for the radar sensing of precipitation," *Radio Science*, vol. 33, no. 5, pp. 1335–1352, 1998, https://onlinelibrary.wiley.com/doi/abs/10.1029/98RS00633.

[65] K. J. Al-Jumily, R. B. Charlton, and R. G. Humphries, "Identification of Rain and Hail with Circular Polarization Radar," *Journal of Applied Meteorology and Climatology*, vol. 30, no. 8, pp. 1075–1087, Aug. 1991, https://journals.ametsoc.org/view/journals/apme/30/8/1520-0450_1991_030_1075_iorahw_2_0_co_2.xml.

[66] T. A. Seliga, R. G. Humphries, and J. I. Metcalf, "Chapter 14 Polarization Diversity in Radar Meteorology: Early Developments," in *Radar in Meteorology*, D. Atlas, Ed. Boston, MA: American Meteorological Society, 1990, pp. 109–114, http://link.springer.com/10.1007/978-1-935704-15-7_14.

[67] D. M. Pozar, "Chapter 9: Theory and Design of Ferrimagnetic Components," in *Microwave Engineering, 4th Edition*, 4th ed. Wiley Global Education, 2012.

[68] A. Ashley, L. F. Marzall, M. Pinto, Z. Popovic, and D. Psychogiou, "Bandwidth design of ferrite-based circulators," in *2018 International Applied Computational Electromagnetics Society Symposium (ACES)*, Mar. 2018, pp. 1–2.

[69] N. K. Nikolova, "Lecture 7: Antenna Noise Temperature and System Signal-to-Noise Ratio," https://www.ece.mcmaster.ca/faculty/nikolova/antenna_dload/current_lectures/L07_Noise.pdf.

[70] A. W. Doerry, "Noise and Noise Figure for Radar Receivers," Sandia National Laboratories, Tech. Rep. SAND2016-9649, 1562649, Sep. 2016, http://www.osti.gov/servlets/purl/1562649/.

[71] F. T. Ulaby and U. Ravaioli, "Chapter 7: Plane-Wave Propagation," in *Fundamentals of Applied Electromagnetics*, 7th ed. New Jersey: Pearson Education, Inc., 2015, pp. 313–351, https://b-ok.cc/book/5156724/0bded7.

[72] R. Baktur, "Chapter 3: Overview of CubeSat Antennas: Design Considerations, Categories, and Link Budget Development," in *Antennas for CubeSats*. Artech House.

[73] P. Lacomme, J.-P. Hardange, J.-C. Marchais, and E. Normant, "23 - THE CHANGING TARGET," in *Air and Spaceborne Radar Systems*, P. Lacomme, J.-P. Hardange, J.-C. Marchais, and E. Normant, Eds. Norwich, NY: William Andrew Publishing, Jan. 2001, pp. 433–443, https://doi.org/10.1016/B978-189112113-5.50025-5.

[74] C. A. Balanis, "Chapter 14: Microstrip and Mobile Communications Antennas," in *Antenna Theory: Analysis and Design*, 4th ed. Hoboken, NJ: John Wiley & Sons, Incorporated, 2016, pp. 783–873, http://ebookcentral.proquest.com/lib/usu/detail.action?docID=4205879.

[75] M. A. Richards, "6. Detection Fundamentals," in *Fundamentals of Radar Signal Processing*. McGraw-Hill Professional, Jun. 2005, https://mhebooklibrary.com/doi/book/10.1036/0071444742.

APPENDICES

APPENDIX A

Antenna Material and Geometry

A.1 Substrate Material

The antennas designed in Chapter 4 and described in this appendix use Rogers ULTRALAM® 2000 as the substrate. Table A.1 provides the substrate's material properties.

Table A.1: Rogers ULTRALAM® 2000 material properties.

Parameter	Value	Units
Dielectric Constant, ϵ_r	2.5	NA
Dissipation Factor, $\tan(\delta)$	0.0022	NA
Substrate Thickness	1.524	mm
Copper Thickness	17	μm

A.2 Corner-Cut Technique

This section presents a descriptive summary of how the corner-cut technique creates a circularly polarized patch antenna and how to analyze and tune the size of the cuts to optimize the antenna characteristics.

Input Impedance of Rectangular and Square Patches

A rectangular patch is one of the most used configuration of a microstrip antenna. Balanis [74] provides equations for the length (l) and width (w) for a rectangular patch with good radiation efficiency. At resonance, the input edge impedance, Z_e, of the patch is purely real. When the the substrate is thin ($h \ll \lambda$), the resonant input edge resistance, R_e, is described by

$$R_e = 90\frac{(\epsilon_r)^2}{\epsilon_r - 1}\left(\frac{l}{w}\right). \tag{A.1}$$

([A.1](#)) shows that increasing the width of the patch decreases the input resistance. Typical values of R_e are $> 150\ \Omega$. To maintain aperture efficiency, the width of the patch is designed to be

$$l \leq w \leq 2l. \tag{A.2}$$

To make a circularly polarized antenna, the corner-cut method uses a square patch. $w = l$ minimizes the size of w and maximizes R_e. Typical values of R_e for a square patch are near $300\ \Omega$.

Circular Polarization with a Square, Corner-Cut Patch

Trimming the corners changes the polarization of the antenna. With the corners cut, the square patch excites two orthogonal modes with $90°$ of phase difference, which make the antenna circularly polarized.

Figure [A.1](#) depicts a circularly polarized patch antenna made with the corner-cut method. The trim, t, makes the path between one set of opposite corners shorter than the path between the untrimmed corners. This causes the mode excited between the trimmed corners to lead in phase. When t is the right size, the amount of phase difference is $90°$ and circular polarization is created.
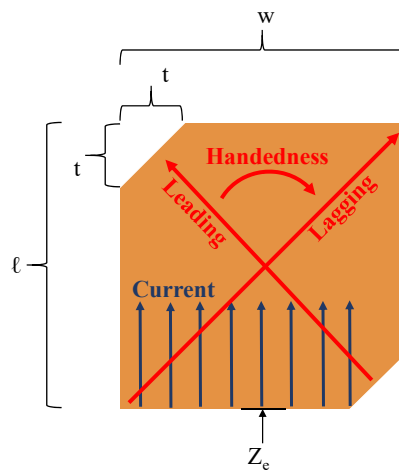

Fig. A.1: Method of determining handedness of corner-cut patch antenna.

The handedness of the antenna depends on which corners are cut. The direction of current on the patch is from the port to the opposite edge. The head of the arrows depicting the modes in Figure A.1 follows the direction of the current and points at the edge opposite the port. By pointing ones fingers along the leading mode with the finger tips at the head of the arrow and curling the fingers towards the head of the lagging mode, the thumb points normal to the patch for the hand that describes the polarization of the patch. This identifies the patch depicted in Figure A.1 as LHCP. Cutting the opposite corners of the patch would result in an RHCP antenna.

Determining t

It is unclear from Balanis [74] how large t should be to create a circularly polarized antenna. Since changing the length of w affects the input resistance of a rectangular patch, it makes sense that trimming the corners does too. Observing the input impedance as well as the axial ratio and cross-polarization levels of the antenna for different sizes of t helps to determine the right t for circular polarization.

As an example, a square patch antenna is designed with $l = w = 31.25$ mm. The Z_e of this square patch is plotted in Figure A.2 as a function of frequency. The resonate frequency is when the imaginary part of Z_e goes to zero. From the results in Figure A.2, the resonate frequency is 2.79 GHz.
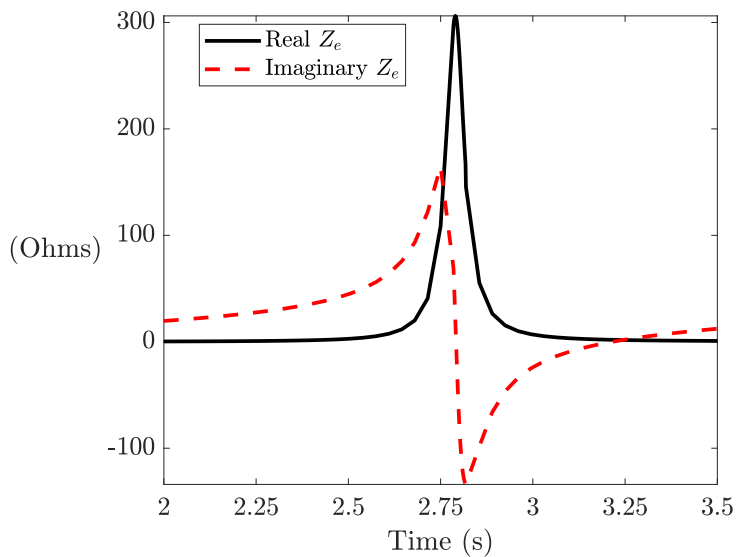
Fig. A.2: Real and imaginary parts of Z_e.

Letting t be proportional to the length of the patch provides the relationship

$$t = \alpha l, \qquad \text{for} \quad 0 \le \alpha \le 0.33. \qquad \text{(A.3)}$$

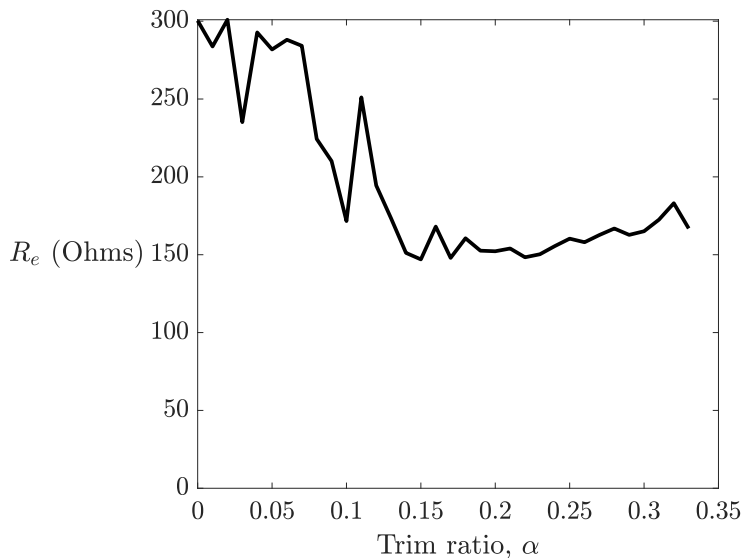For various values of the constant of proportionality, α, Figure A.3 shows the value of R_e.

Fig. A.3: Resonant edge resistance for various trim sizes.

R_e is over 300 Ω when the corners are whole. As α increases, R_e decreases until it settles at about 150 Ω or half of the original edge resistance. Before examining how well the patch behaves like an antenna, the patch needs to be matched to the feed structure. 300 Ω and 150 Ω are difficult to match with a microstrip line using the resources available at Utah State University, so matching is accomplished by using a probe feed. The probe inset distance, y_0, is calculated as follows [74]

$$R_{in}(y = y_0) = R_{in}(y = 0)cos^2\left(\frac{\pi}{l}y_0\right)$$
$$R_p = R_0 cos^2\left(\frac{\pi}{l}y_0\right)$$
$$y_0 = \frac{l}{\pi}cos^{-1}\left(\sqrt{\frac{R_p}{R_0}}\right), \tag{A.4}$$

where:

$R_{in}(y = y_0), R_p = $ input resistance of probe [Ω]

$R_{in}(y = 0), R_0 = $ input resistance at edge of patch [Ω].

The result of (A.4) is $y_0 = 11.4$ mm. After tuning in Ansys HFSS®, $y_0 = 10.7$ mm is applied.

The corners of the patch are then trimmed and the input impedance at the probe, Z_{in}, is observed. Figure A.4 shows Z_{in} for frequencies around the resonant frequency at various values of α.
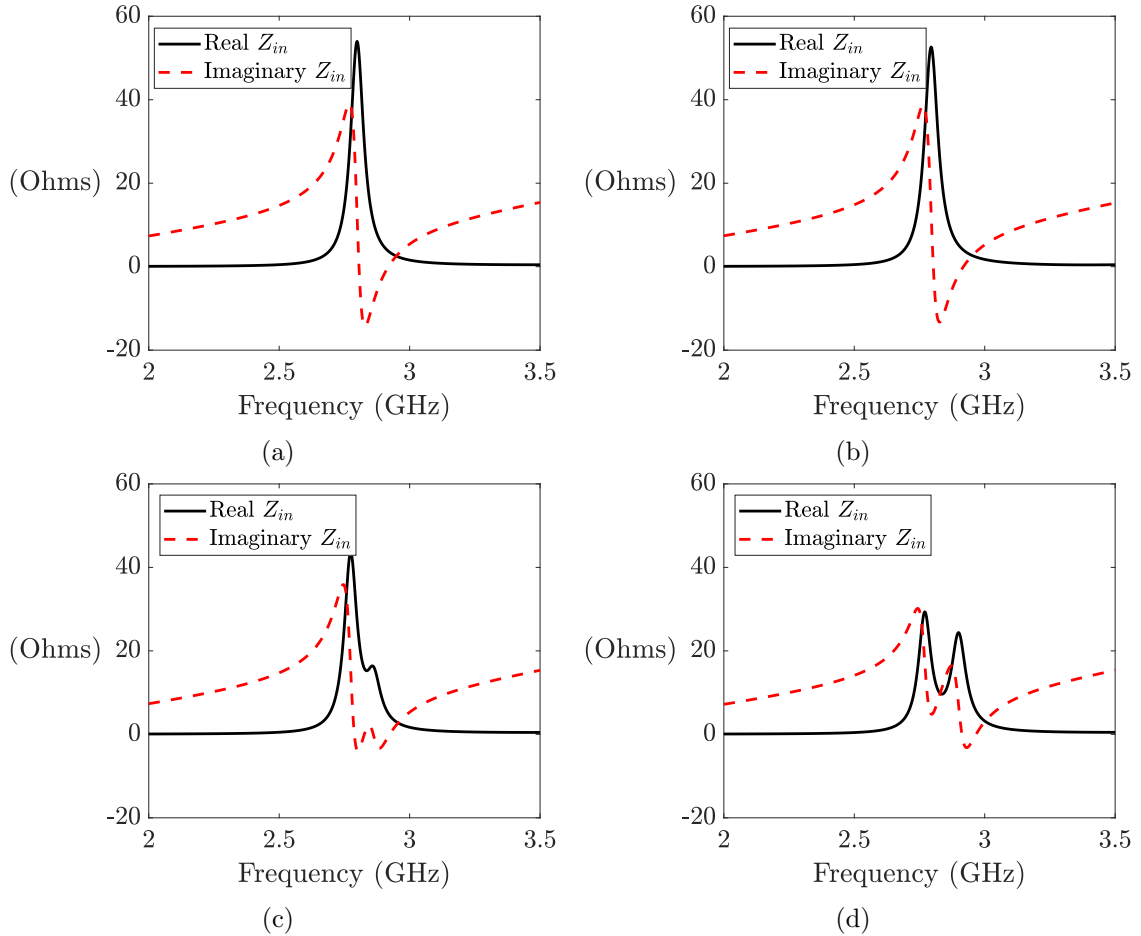
Fig. A.4: Z_{in} for different trim ratios: (a) $\alpha = 0.0$ (b) $\alpha = 0.05$ (c) $\alpha = 0.1$ (d) $\alpha = 0.15$.

With no trim (Figure A.4a) and a small trim (Figure A.4b), there is only one resonant frequency. When the trim is large enough, the real Z_{in} begins to split into two peaks (Figure A.4c). This shows that two frequencies are resonating in the patch. The higher frequency is a result of the shorter distance between the trimmed corners. As the trim ratio is enlarged further, the peaks separate and distinctly show two resonant frequencies (Figure A.4d).

While the visualization in Figure A.4 is helpful to understand how cutting the corners of a square patch makes multiple resonant modes, it is not enough to show circular polarization; for that, the axial ratio and cross-polarization need to be considered as well. A linearly polarized antenna has a large (ideally infinite) axial ratio. A perfectly circularly polarized

antenna has an axial ratio of 1 (0 dB). In practice, circular polarization has an axial ratio < 3 dB and linear has an axial ratio > 30 dB [22]. Anything else is characterized as elliptically polarized. A good circularly polarized antenna has a cross-polarization > 20 dB.

The axial ratio and cross-polarization of the patch antenna for four trim ratios is shown in Figure A.5.
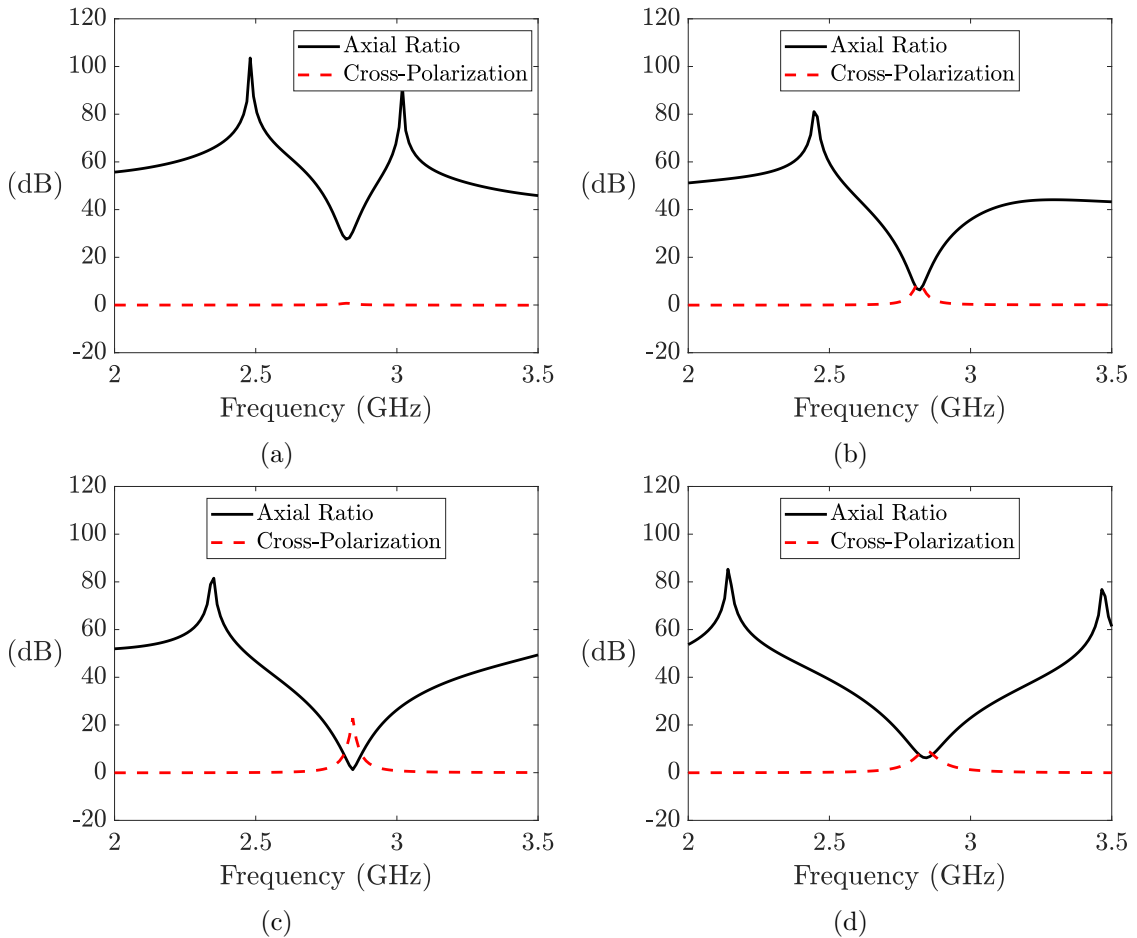

Fig. A.5: Axial ratio and cross-polarization for different trim ratios: (a) $\alpha = 0.0$ (b) $\alpha = 0.05$ (c) $\alpha = 0.1$ (d) $\alpha = 0.15$.

As expected, Figure A.5a is linearly polarized. Because the axial ratio of Figure A.5b is below 30 dB, it depicts an elliptically polarized antenna. Figure A.5c is circularly polarized and has a cross-polarization of 23 dB. Despite the two resonant frequencies in Figure A.4d, Figure A.5d is elliptically, not circularly, polarized. This demonstrates that two resonant

frequencies alone is not enough for circular polarization. The resonant frequencies need to be near each other to couple properly.

Another observation is that the frequency with the lowest axial ratio in Figure A.5c (2.84 GHz) is not one of the two resonant peaks shown in Figure A.4c. Instead, the lowest axial ratio is found approximately midway between the resonant peaks.

Referring back to Figure A.3, $R_e = 170$ Ω for the 0.1 trim ratio that produces circular polarization in Figure A.5c. This shows that the best circular polarization parameters come before R_e settles. The trim ratio should be chosen so that R_e is near, but still greater than, half the original edge resistance. Also, knowing the edge resistance of the corner-cut patch that provides the best circular polarization, (A.4) can be used to calculate a new y_0 that will provide a better match.

A.3   2.4 GHz Antenna Geometry

The dimensions, trim size, and feed location of the patch antenna described as an example in Appendix A.2 are tuned until the patch behaves like a circularly polarized antenna at 2.4 GHz. Figure A.6 shows the geometry of the LHCP patch antenna, and Table A.2 provides values for each dimension. The size in wavelengths assumes an operating frequency of 2.4 GHz. y_0 is such that $Z_{in} = 50$ Ω. It is worth noting that the trim ratio for this antenna is 0.09 which is near the ratio of 0.1 found in Appendix A.2. All of the RHCP dimensions are comparable.
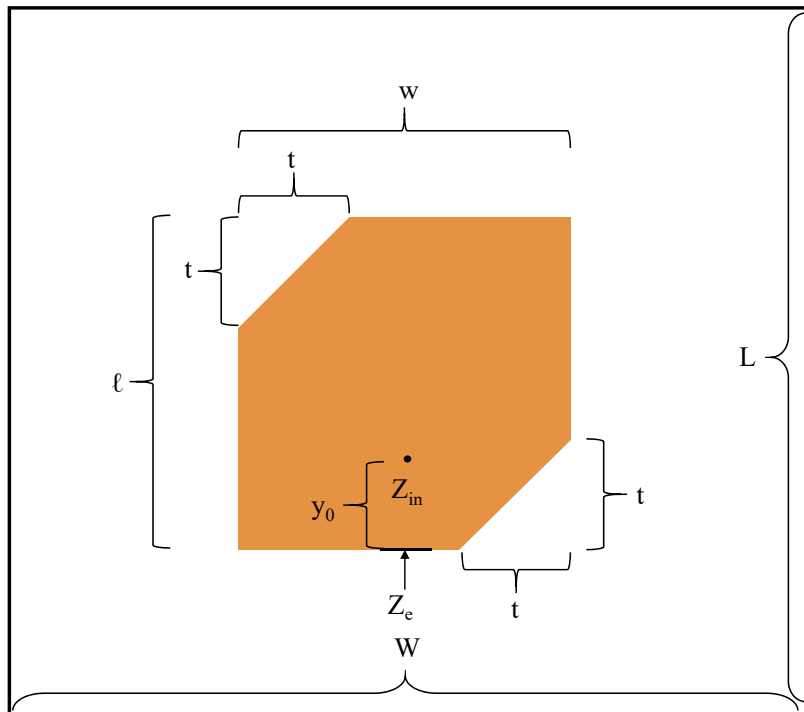
Fig. A.6: Geometry of circularly polarized patch antenna.

Table A.2: Dimensions from Figure A.6 in both physical size and number of wavelengths.

Parameter	Label	Size (mm)	Size (λ)
Length of Ground Plate	L	125	1
Width of Ground Plate	W	125	1
Length of Patch	l	38.125	0.305
Width of Patch	w	38.125	0.305
Length of Trim	t	3.5266	0.028
Feed Inset Distance	y_0	11	0.88

Figure A.7 shows Z_{in} for the antenna described by Figure A.6 and Table A.2. For convenience and comparison, Figure 4.4 is copied here as Figure A.8 to show the axial ratio and cross-polarization of this antenna design.
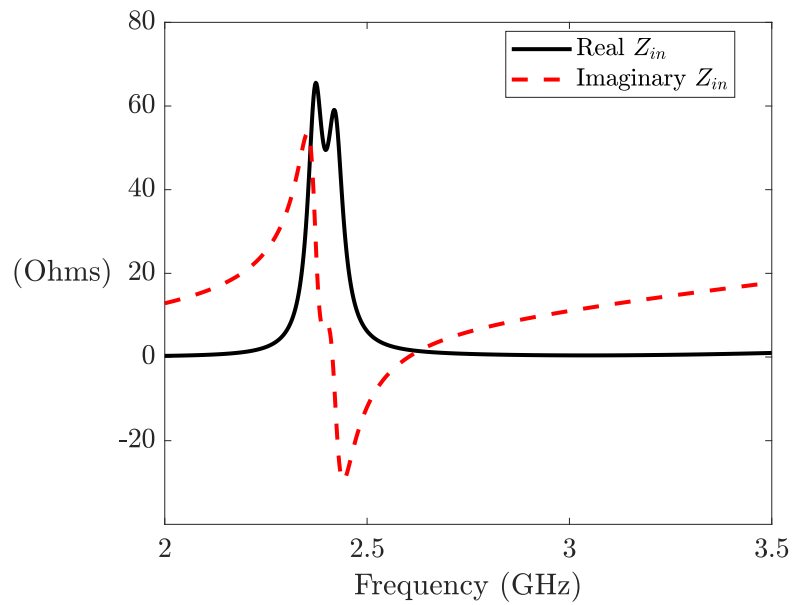
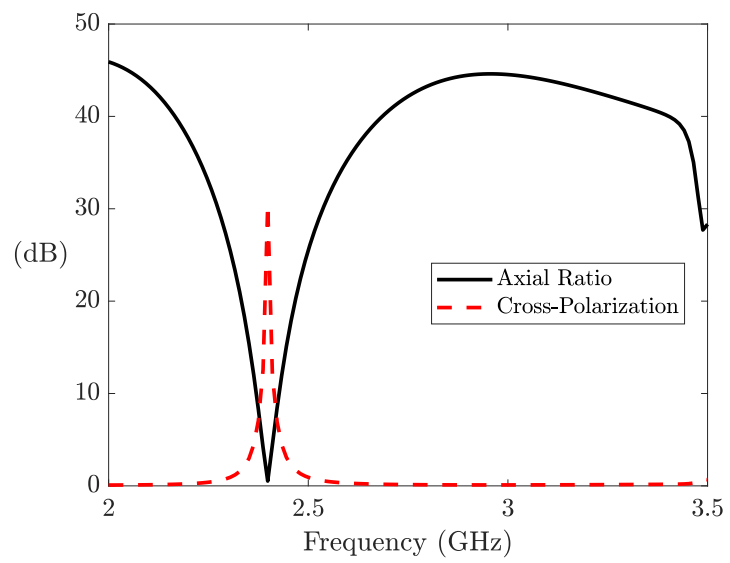Fig. A.7: Z_{in} of the antenna described by Figure A.6 and Table A.2.

Fig. A.8: Axial ratio and cross-polarization of the antenna from Figure A.6 and Table A.2.

APPENDIX B

Detection and False-Alarm Probabilities

The SNR design requirement for a receiver is chosen based on the desired probability of detection (P_d) and probability of false-alarm (Pfa). The relationship between the SNR, P_d, and Pfa is shown in Figure B.1 for nonfluctuating targets and Figure B.2 for fluctuating targets. Further derivations and calculations can be found in [30, 75]
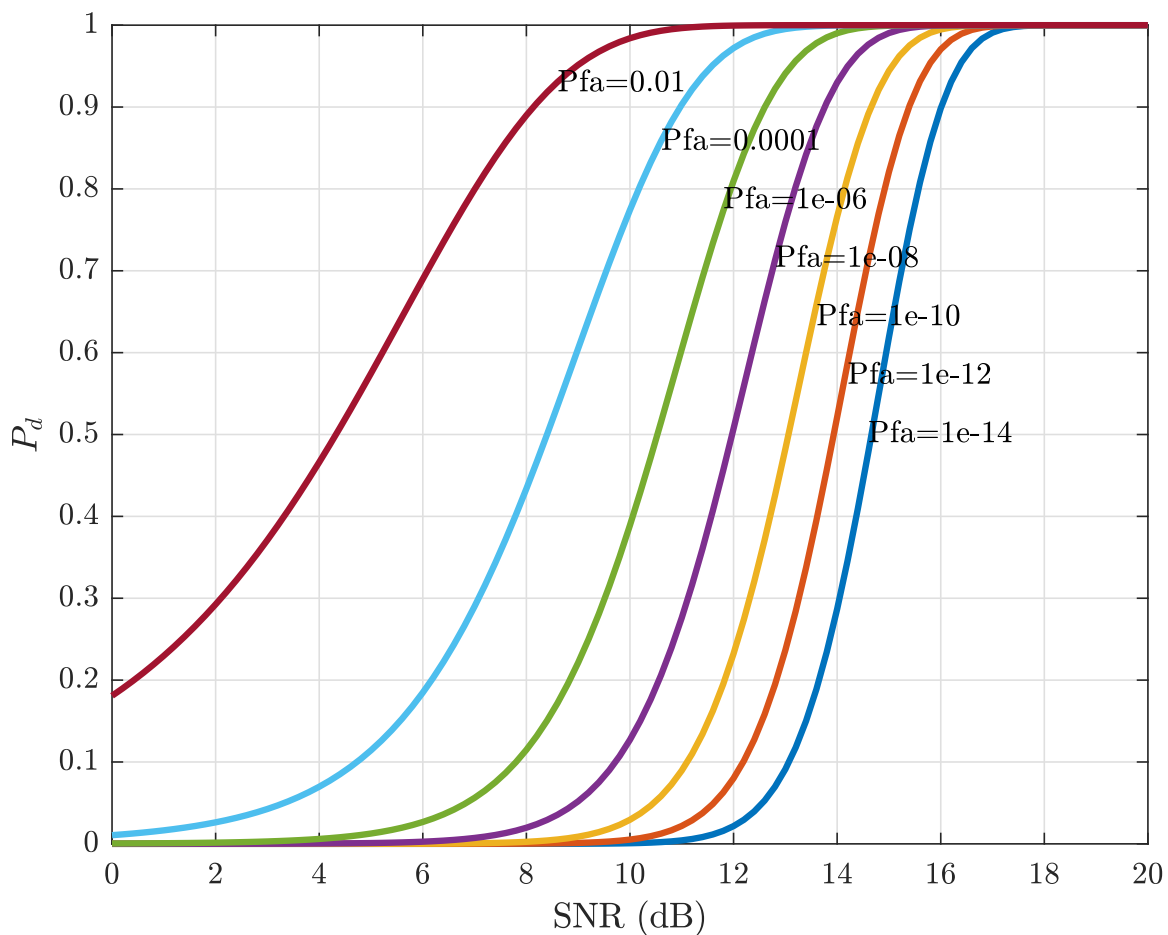

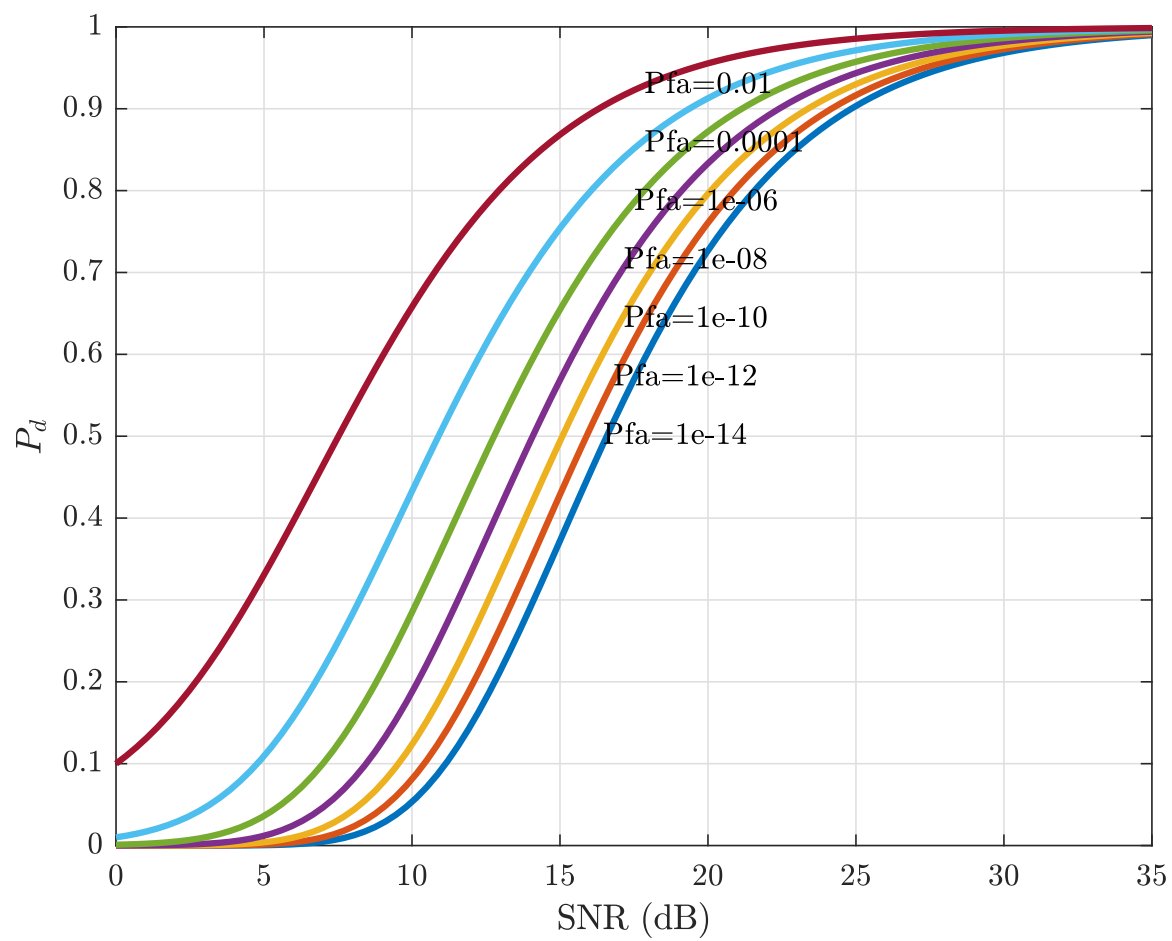Fig. B.1: Probability of detection based on SNR for a non-fluctuating target.

Fig. B.2: Probability of detection based on SNR for a fluctuating target.

APPENDIX C

Radar-Front-End Components

The components in the radar front-end from Section 6.4 are shown explicitly in Table C.1.

Table C.1: Part numbers of components in the radar front-end shown in Section 6.4.

Component Label	Manufacturer	Part Number
LNA	Mini-Circuits	ZX60-272LN-S+
MIX	Mini-Circuits	ZX05-30W
VCO	Mini-Circuits	ZX95-2500
BPF	KR Electronics, Inc.	KR 2722

Mini-Circuits has made the exact part numbers obsolete for the mixer and VCO listed in Table C.1. At the time of publication of this thesis, the updated part numbers are ZX05-30W-S+ and ZX95-2500-S+ respectively.

A datasheet for each component is accessible on the manufactures' websites. The Mini-Circuits website is https://www.minicircuits.com. The KR Electronics, Inc. website is https://krfilters.com.